COMPUTATIONAL MODELING AND OPTIMIZATION OF A NOVEL SHOCK TUBE TO STUDY BLAST INDUCED TRAUMATIC BRAIN INJURY

A Thesis

by

PRATIMA ANUMOLU

Submitted to the Office of Graduate and Professional Studies of
Texas A&M University
in partial fulfillment of the requirements for the degree of

MASTER OF SCIENCE

Chair of Committee,	Michael R. Moreno
Committee Members,	John C. Criscione
	Devesh Ranjan
	Raoul van Loon
Head of Department,	Gerard Cote

August 2014

Major Subject: Biomedical Engineering

ABSTRACT

Over the last decade, soldiers fighting in Iraq and Afghanistan are being exposed to blasts from powerful explosives with improvised detonation techniques. These blasts put them at high risk of closed head non-impact Blast-induced Traumatic Blast Injury (bTBI). bTBI is caused by interaction of shock-wave. It is a debilitating condition, but goes undiagnosed for several months. The pathology of bTBI is poorly understood making diagnosis, treatment, and prevention of bTBI difficult. One way to study it is to construct a shock tube that replicate blast profile. However, this method does not replicate blast conditions perfectly. The goal of this research is to improve shock tube as a research tool, for studying bTBI, by better replicating military ordnance.

Various 2D models to simulate the shock wave propagation in a shock tube to see the effects of varying shock tube geometry and working fluid on the blast profiles were developed. Ranges of different parameters evaluated are: tube length - 5ft to 25ft; tube diameter - 8" to 16"; working fluid - compressed air and helium; burst pressure- 20 to 55 psi. A total of 240 simulations were run to evaluate the effect of these factors on the pressure profile. Computations were carried out using commercial software, Star CCM+ (CD-adapco, NY, USA). Assumptions used to model the flow were unsteady, inviscid, compressible, axisymmetric flow with time-step of $1e^{-5}$s. Multiple regression was run on these parameters to establish empirical relationship with pressure profile. CFD model was validated using experimental data from Robbins-Moreno shock tube.

Results show that as the burst pressure increases, peak overpressure, positive phase duration, and impulse also increase. Increasing tube diameter decreases peak. Change in tube length does not have a significant effect on peak overpressure, positive phase duration, and impulse. Working fluid was most significant factor determining the magnitude of impulse and duration.

In conclusion, the empirical formulas developed using CFD model of the shock tube provide reasonable predictions about the key features of a pressure profile that and their dependence on the shock tube geometry, working fluid, and burst pressure. This knowledge will be used to improve shock tube to study bTBI.

DEDICATION

I would like to dedicate this thesis to……

My parents and my sister

And

All the Soldiers serving at home and abroad

ACKNOWLEDGEMENTS

To my Guru, Dr Michael Moreno: Thank you for all of the love and support. Thank you for letting me be part of your lab.

Christie Bergerson, Caleb Davis, James Peterson, Andrew Robbins, and Steve Zambrano: thank y'all for making my journey so much fun and extraordinarily memorable.

Dr. Raoul van Loon: Thank you so much for your support throughout the course of this research.

I would like to thank my committee members, Dr. John Criscione, and Dr. Devesh Ranjan, for their support.

Thanks also go to my friends and colleagues and the department faculty and staff for making my time at Texas A&M University a great experience.

Finally, thanks to my family for their encouragement, patience, and love.

NOMENCLATURE

bTBI	Blast-induced Traumatic Brain Injury
FDM	Finite Difference Method
FVM	Finite Volume Method
AUSM	Advection Upstream Splitting Method
DOE	Design of Experiments

TABLE OF CONTENTS

Page

Page

Page

LIST OF FIGURES

Page

Page

Page

. Page

LIST OF TABLES

Page

Page

CHAPTER I

THESIS OVERVIEW

There are six chapters in this thesis, which cover various, computational and optimization topics related to the shock tube and blast-induced traumatic brain injury (bTBI). Main topics of each chapter are discussed in the following paragraphs:

Chapter two covers motivation behind this research and the need to study bTBI. Current knowledge and understanding of bTBI research is outlined. Characteristics of a typical open field detonation have also been included. The theory behind a shock tube and shock wave diagrams is included to gain better understanding of blast wave physics.

Chapter three covers the review of current state of numerical schemes for modelling compressible Euler equations in terms of their fundamental properties for one-dimensional shock tube. It compares them in terms of accuracy, efficiency, and ease in implementation.

Chapter four investigates development of 2D computational model to simulate the shock wave propagation in shock tube at Biomechanical Environments Lab (BMEL), and presents a comparison between a fully-ruptured membrane model with half-ruptured membrane model.

Chapter five covers the optimization of Robbins-Moreno shock tube. Computational modeling and statistical analysis were used to determine empirical relations between tube length, tube diameter, burst pressure, working fluid with blast wave, specifically peak overpressure, positive phase duration, and positive impulse.

Chapter six summarizes important results obtained in each chapter. Also, included in this chapter is a list of recommendation for experiments for future work to be done at TAMU's Biomechanical Environments Laboratory.

The references sections and appendices are included after the main body of the thesis.

CHAPTER II

MOTIVATION AND BACKGROUND

2.1 Blast-induced Traumatic Injury

Center for Disease Control defines a Traumatic Brain Injury (TBI) as a bump, blow or jolt to the head or a penetrating head injury that disrupts the normal function of the brain. As of 2010, an estimated 2.5 million people suffer from TBI. Historically, the common causes of TBI have either been sports, motor accident, and/ or falls. Hence, these types of injuries have been rigorously studied. However, in recent times, occurrence of Blast-induced Traumatic Brain injury (bTBI) has seen a sharp rise.

Since 2001, more than two million U.S. military personnel have been deployed to Iraq and Afghanistan [1]. Our soldiers fighting in Operation Enduring Freedom and Operation Iraqi Freedom are exposed to blasts that are growing increasingly powerful every day. These explosives also employ innovative detonation techniques, putting them at high risk for Blast-induced Traumatic Blast Injury (bTBI). As of 2013, the Veterans Affairs (VA) has reported 56,695 Iraq and Afghanistan war veterans enrolled with VA healthcare for being either assessed or treated for conditions related to bTBI [2].

Due to improvement in protective gear, a higher number of soldiers are surviving injuries due to shrapnel, which was otherwise fatal in past wars. However, as the blast wave passes through the body, it transfers immense amount of kinetic energy, which causes damage to the brain. Many times these injuries are “closed-head”. In a closed head injury, the brain actually is jostled around, but there is no apparent skull fracture.

Often times in combat zones, bTBI occurs simultaneously with more obvious and visible life-threatening injuries, therefore, cases may go unrecognized. When bTBI occurs with no outward signs of trauma, soldiers might not even seek medical treatment. The cumulative effects of repeated exposure can also be very problematic and go undiagnosed for several months. Most common symptoms for bTBI include severe headaches, difficulty sleeping, and mood swings, symptoms that may or may not be related to concussion [1]. Based on the mechanism of injury, bTBI is summarized into four subcategories [3, 4]. Figure 2:1 presents a summary of the classification.

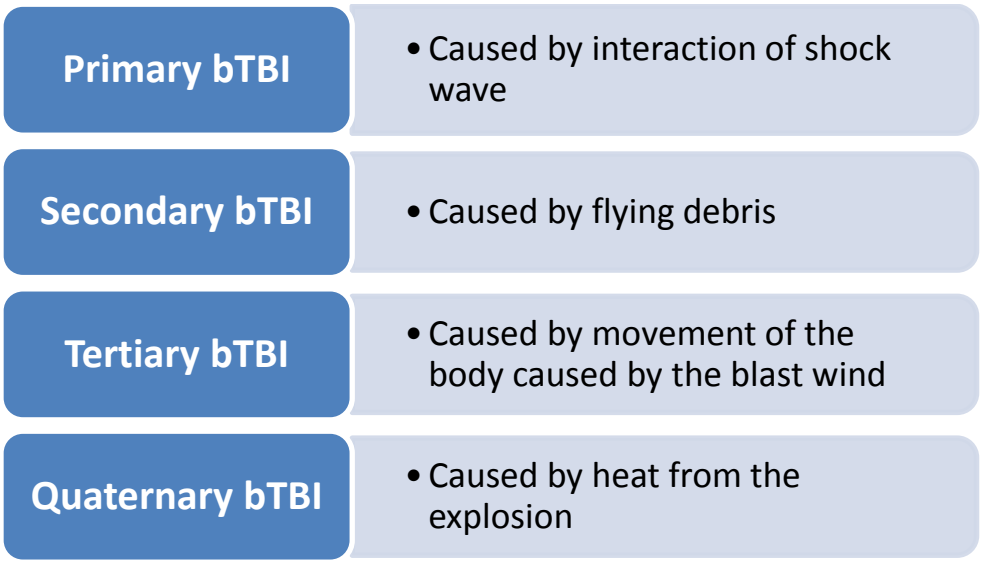

Figure 2:1 Classification of Blast-induced Traumatic Brain Injury

Despite the dangers presented by bTBI to our military personnel, the epidemiology of bTBI is poorly understood. Even with current imaging technology, bTBI is not always immediately detected [5]. What we understand so far is that characteristics of blast

induced TBI is distinct in comparison to concussion [4]. The biggest obstacle in finding diagnosis, treatment, and prevention of bTBI is lack of understanding of bTBI pathology. To understand the effects of exposure to blast waves, current investigation encompasses use of animal models, small as well large [6-9]. These models are exposed to blast wave either using chemical explosive or shock tubes [10]. Shock tubes replicate explosives' blast pressure profile in laboratory setting in a controlled way.

2.2 Shock Tube

2.2.1 Blast Wave

Detonation of an explosive causes deposition of energy, creating a pressure gradient, which generates a shock wave. Friedlander's wave [11] illustrates a typical pressure profile of a wave generated by an explosion as seen in Figure 2:2. When an explosion occurs, there is a sudden and sharp rise over the atmospheric pressure, p_o, above normal to reach a maximum overpressure, p_s. The peak overpressure varies between explosives. This is followed by exponential decay of the initial positive overpressure below the atmospheric pressure. Finally, the wave returns to atmospheric pressure.

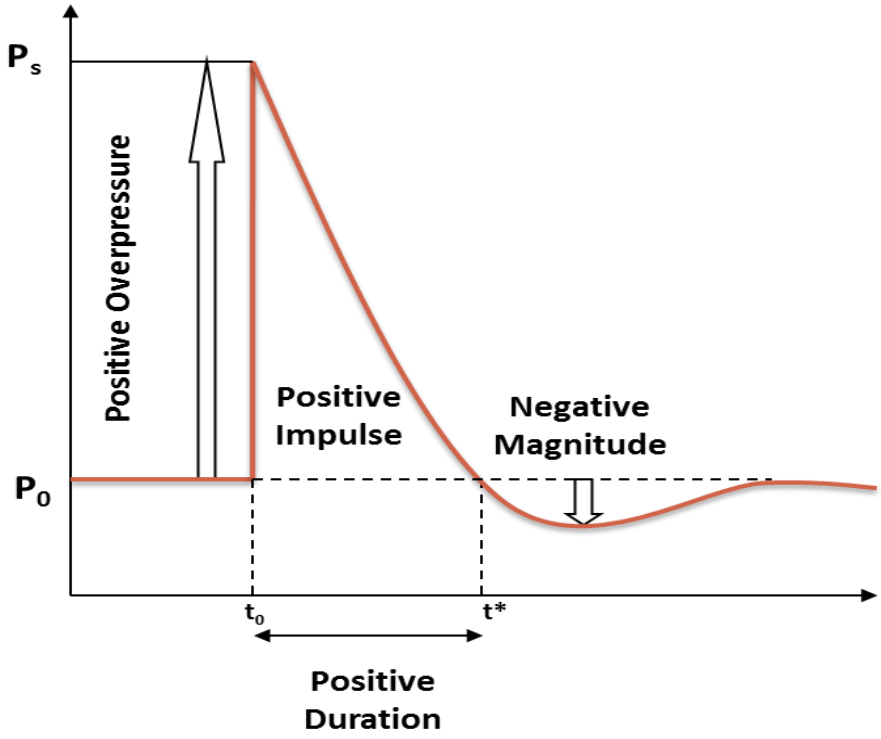

Figure 2:2 T_o is the Time at Which Pressure Begins to Rise Above Atmospheric Pressure P_o and Reaches Peak Pressure P_s. t^* is the Time When Pressure Plummets Below Atmospheric Pressure

2.2.2 Theory Behind a Shock Tube

Shock tubes can be used to generate blast-shock waves in the laboratory (see Figure 2:3). Depending on the application, one can use either an open-ended shock tube or a close-ended shock tube. The tube has two sections: Driver section, and Driven section. The driver section (region 4) is maintained at a higher pressure in comparison to the driven section (region 1). These sections are separated using a membrane. The gas in the two sections can be either same or different [11].

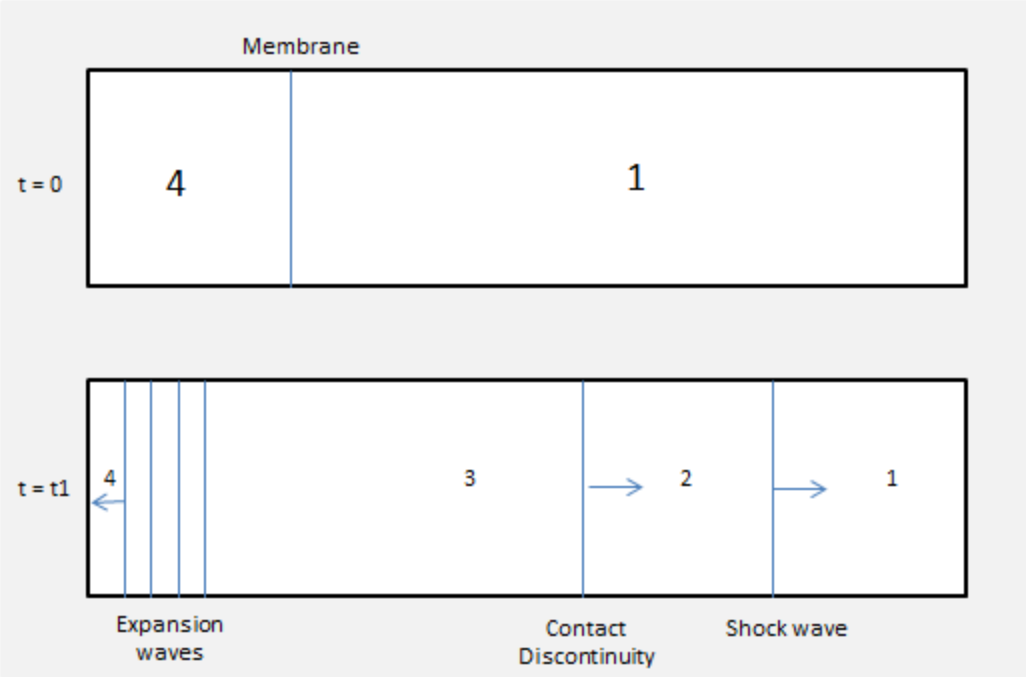

Figure 2:3 Shock Tube Operation

Analytical model describing pressure, velocity for shock tube is described below [12]:

In regions separating Zone 1-4,

Speed of sound through gas, $a = \sqrt{\frac{P\gamma}{\rho}}$ …..**(2-1)**

Zone 2

Velocity: $u_2 = \frac{a_1}{\gamma}\left(\frac{p_2}{p_1} - 1\right)\sqrt{\left(\frac{2\gamma/(\gamma+1)}{p_2/p_1 + (\gamma-1)(\gamma+1)}\right)}$ **…...(2-2)**

Shock wave speed: $V_s = a_1\sqrt{\frac{\gamma+1}{2\gamma}\left(\frac{p_2}{p_1} - 1\right) + 1}$ **……(2-3)**

In region separating zone 3 and 4,

$$\frac{p_3}{p_4} = \left(\frac{\rho_3}{\rho_4}\right)^{\gamma_4} == \left(\frac{a_3}{a_4}\right)^{\frac{2\gamma_4}{(\gamma_4 - 1)}} \qquad \textbf{…..(2-4)}$$

Relation between ratio of p_4/p_1 and p_2/p_1 is defined as,

$$\frac{p_4}{p_1} = \frac{p_2}{p_1}\left[1 - \frac{(\gamma_4 - 1)\left(\frac{a_1}{a_4}\right)\left(\frac{p_2}{p_1} - 1\right)}{\sqrt{2\gamma_1}\sqrt{2\gamma_1 + (\gamma_1 + 1)(\frac{p_2}{p_1} - 1)}}\right]^{-[2\gamma_4/(\gamma_4 - 1)]} \qquad \textbf{….(2-5)}$$

Shock strength is defined as p_2/p_1. Generally, we are looking to solve for this, given diaphragm ratio, p_4/p_1. Solving for p_2/p_1 is non-linear, making the shock tube computationally complex.

2.2.3 Placement of Animal Model for Blast Wave Exposure

Shock tubes are a common experimental model used to induce brain injury in animal model to gain better understanding of pathology of bTBI. The animal models can be placed either inside or outside the shock tube to expose it to the blast wave. A considerable amount of variation is seen in pressure profiles and peak overpressure along the shock tube. Risling et. al. placed animal model inside the tube, 1 m away from diaphragm and exposed them to peak pressure waves of 130 and 260kPa [13]. Bauman et. al. studied closed head injury by using swine model that were placed inside the shock tube 44ft. from the end of the tube [7]. Long et. al. recreated the injury in rats by placing them in a holder just outside the mouth of the shock tube [14].

Friedlander wave provides description of an open field detonation that originates from a radial source and propagates radially. These shock wave propagation have a three dimensional flow field with significant curvature near the origin of blast. Exposure to blasts at such proximity would be lethal, taking into account the improved explosive devices. Most of the mild bTBI is caused due to far-field exposure to the blasts. Hence, focus of bTBI research is recreate fair-field exposure blast conditions. As distance increases from origin of explosions, the waves are more planar.

Shock tubes generate blast waves that are planar at the open-end. Within the shock tube, shock waves propagate in a single direction resembling a Friedlander wave. But, as soon as the waves exit the tube, they propagate in all directions.

Based on literature review, it was concluded that that positioning animal model inside the shock tube rather than outside the tube, provides a better replication of open field detonation to cause mild to moderate bTBI.

2.2.4 A Novel Shock Tube at TAMU's Biomechanical Environments Lab

In our laboratory, we are using an MRI compatible open-ended shock tube such that the initial pressure in the driven section is atmospheric. The driven section is separated from driver section using a Mylar membrane. In order to generate a blast wave with the basic features of a Friedlander wave, driver section is pressurized and at a specified burst pressure, membrane is ruptured mechanically. Mechanically rupturing the membrane causes instant propagation of the blast wave. Figure 2:4, Figure 2:5, and Figure 2:6 describe the placement of animal in the shock tube.

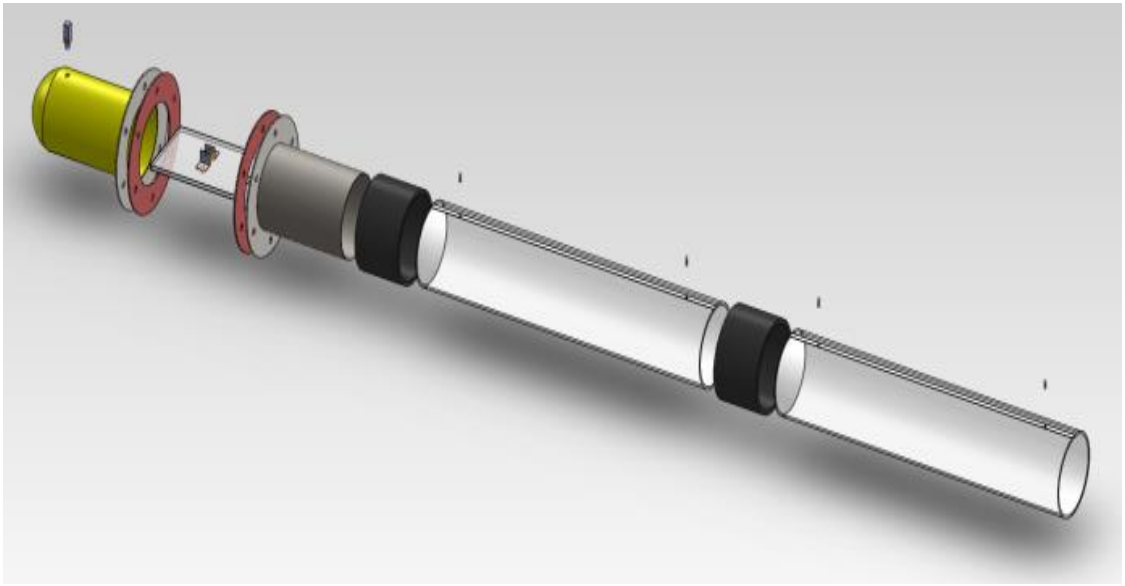

Figure 2:4 Solidworks of Robbins-Moreno Shock Tube

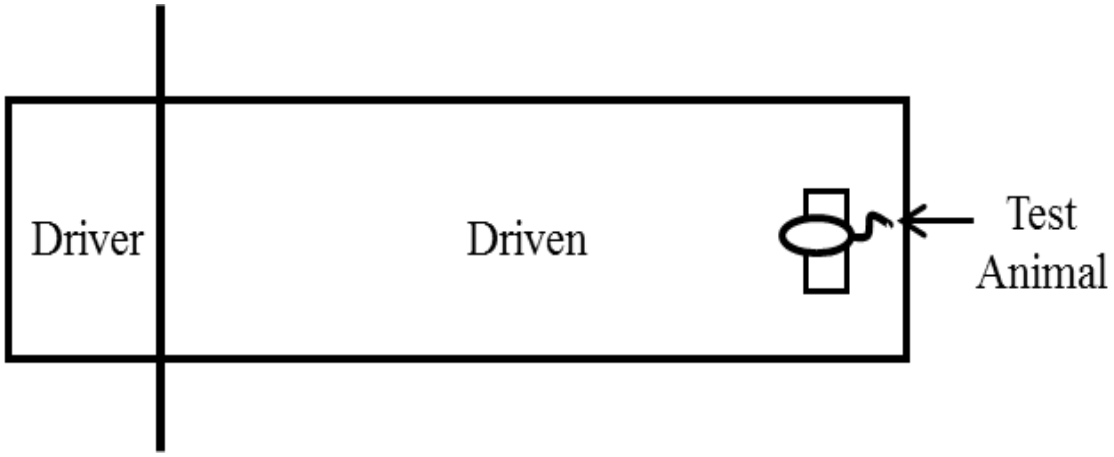

Figure 2:5 Placement of Test Animal in Shock Tube

Figure 2:6 Robbins-Moreno Shock Tube and Placement of Test Animal in Our Shock Tube

Figure 2:6 Continued

2.3 Research Objective

Even though bTBI has been well studied in recent years, there is still need for better experimental and computational models. The shock tube has been one of the most commonly used experimental models of blast in biomedical research. However, this method does not replicate blast conditions perfectly. The specific deficiencies in bTBI research are as follows [15-19]:

1. Pathophysiology dependent on blast wave: Effect of the blast on the brain has only been studied as with respect to peak overpressure of the blast wave. However, contribution of the other features of blast wave have not been well studied.

2. Inconsistency in the data: Shock tubes have been widely used to study blast related injuries. However, blast profiles inconsistent with any standard for exposure, result in misleading data.

Our research focuses on improving the shock tube as a research tool, for studying bTBI, by better replicating military ordnance.

CHAPTER III

ONE DIMENSIONAL SHOCK TUBE

3.1 Introduction

3.1.1 Objective

Several schemes to model Euler equation have already been developed, implementing both finite difference methods and finite volume methods. A review of some of the most common schemes is presented. The scheme needs to be robust enough to capture the shock as well as be efficient. The current state of scheme for compressible Euler equation of fundamental properties of the different modeling schemes for one-dimensional shock tube is reviewed. These schemes will later studied for coupling with a Fluid-Structure interaction model of the brain.

Current state of schemes for numerical modelling of Euler equation for unsteady, compressible, inviscid, perfect gas, and investigate accuracy of shock capturing will be reviewed. To answer these questions, numerical modeling will be used in order to investigate the effect of the schemes.

3.1.2 Governing Equations

For an unsteady, compressible, inviscid perfect gas

$$\frac{\partial}{\partial t}\begin{bmatrix}\rho\\ \rho v\\ E\end{bmatrix}+\frac{\partial}{\partial x}\begin{bmatrix}\rho v\\ \rho v^2+p\\ v(E+p)\end{bmatrix}=0 \ldots\ldots\ldots (3.1)$$

Substituting,

$$\boldsymbol{Q = \begin{bmatrix} \rho \\ \rho v \\ E \end{bmatrix} \quad and \quad F = \begin{bmatrix} \rho v \\ \rho v^2 + p \\ v(E + p) \end{bmatrix} = 0}$$

Therefore, Eq (1) can be rewritten as:

$$\mathbf{\frac{\partial}{\partial t} Q + \frac{\partial}{\partial x} F = 0} \ldots\ldots\ldots (\mathbf{3.2})$$

where,

$$\mathbf{\rho = density}$$

$$\mathbf{v = velocity}$$

$$\mathbf{p = pressure}$$

$$\mathbf{E = Energy}$$

Equation of State for perfect gas,

$$\mathbf{p = (\gamma - 1)\left(E - \frac{1}{2}\rho v^2\right)} \ldots\ldots\ldots\ldots (\mathbf{3.3})$$

Where,

$$\mathbf{\gamma = Gamma\ (1.4\ for\ air)}$$

3.2 Method

The computational domain has a total length of 1 m. The left side of the domain with length of 0.5 m is a high-pressure region. The right side of the domain has a length of 0.5m, is a low-pressure region. The initial conditions are listed in Table 3:1.

Table 3:1 Initial data for driver section and driving section used for evaluating numerical schemes for 1D Euler equation

	Left Domain	**Right Domain**
Pressure, p [Pa]	1	0.125
Density, ρ [kg/m^{3}]	1	0.1
Velocity, u [m/s^{2}]	0	0
Gamma	1.4	
Tube length [m]	1	
Membrane Position [m]	0.5	

MATLAB was used to compare various finite difference methods and finite volume methods. The hardware used is Intel Core i3-2350 at 2.3 GHz with dual core server processor. The effect of grid resolution was evaluated by varying grid points, N as 101, 601, and 1001. The relative L1 norm error with respect to exact solution was calculated. Effect of CFL number at 0.1 and 0.95 on finite difference method was also evaluated. Listed below are the various numerical schemes that were compared for solving 1D compressible Euler Equations.

3.2.1 Finite Difference Method

Following methods obtain numerical solution by discretizing the geometric domain into nodes:

3.2.1.1 Lax-Friedrich

Conservative form of Lax-Friedrich's scheme is proposed as following to solve the above (eq 3.1) Euler Equations [20]:

$$\mathbf{Q_j^{n+1} = \frac{1}{2}\left(Q_{j+1}^n + Q_{j-1}^n\right) - \frac{\Delta t}{2\Delta x}\left(F_{j+1}^n - F_{j-1}^n\right) \ldots\ldots\ldots (3.4)}$$

3.2.1.2 Lax-Wendroff

Two step Lax- Wendroff scheme is presented below:

First Step:

$$\mathbf{Q_j^* = \frac{1}{2}\left(Q_j^n + Q_{j+1}^n\right) - \frac{\Delta t}{2\Delta x}\left(F_{j+1}^n - F_j^n\right) \ldots\ldots\ldots (3.5)}$$

Second Step:

$$\mathbf{Q_j^{n+1} = Q_j^n - \frac{\Delta t}{\Delta x}\left(F_{j+1/2}^* - F_{j-1/2}^*\right) \ldots\ldots\ldots (3.6)}$$

Where F* is intermediate solution. It is second-order accurate in both time and space **[**21]

3.2.1.3 MacCormack

MacCormack scheme is presented below:

$$\mathbf{Q_j^* = Q_j^n - \frac{\Delta t}{\Delta x}\left(F_{j+1}^n - F_j^n\right) \ldots\ldots\ldots (3.7)}$$

$$\mathbf{Q_j^{n+1} = \frac{1}{2}\left(Q_j^n + Q_j^*\right) - \frac{\Delta t}{2\Delta x}\left(F_j^* - F_{j-1}^*\right) \ldots\ldots\ldots (3.8)}$$

It is a variation of Lax-Wendroff Scheme, and same as Lax-Wendroff in linear case.

3.2.1.4 Richtmyer

Richtmyer Scheme is presented below: [22]

$$\mathbf{Q}_{j+1/2}^{n+1/2} = \frac{1}{2}\left(\mathbf{Q}_j^n + \mathbf{Q}_{j+1}^n\right) - \frac{\Delta t}{2\Delta x}\left(\mathbf{F}_{j+1}^n - \mathbf{F}_j^n\right) \ldots\ldots\ldots (3.9)$$

$$\mathbf{Q}_j^{n+1} = \mathbf{Q}_j^n - \frac{\Delta t}{\Delta x}\left(\mathbf{F}_{j+1/2}^{n+1/2} - \mathbf{F}_{j-1/2}^{n+1/2}\right) \ldots\ldots\ldots (3.10)$$

It is also a variation of two-step Lax-Wendroff scheme.

3.2.2 Finite Volume Method

Following methods obtain numerical solution by subdividing the geometric domain into small control volume and assigns computational node to the control volume center:

3.2.2. 1 Van Leer

In Van Leer scheme, the numerical flux is written as:

$$\mathbf{Q}_{j+1/2} = \mathbf{F}_j^n + \mathbf{F}_{j+1}^n \ldots\ldots\ldots (3.11)$$

And the vector splitting is as follows:

$$F^+ = \frac{\rho c}{4}(M+1)^2 \begin{bmatrix} 1 \\ \frac{2c}{\gamma}\left(1 + \frac{\gamma-1}{2}M\right) \\ \frac{2c^2}{\gamma^2-1}\left(1 + \frac{\gamma-1}{2}M\right)^2 \end{bmatrix} \ldots\ldots\ldots (3.12)$$

$$F^- = \frac{\rho c}{4}(M+1)^2 \begin{bmatrix} 1 \\ \frac{2c}{\gamma}\left(-1 + \frac{\gamma-1}{2}M\right) \\ \frac{2c^2}{\gamma^2-1}\left(1 - \frac{\gamma-1}{2}M\right)^2 \end{bmatrix} \ldots\ldots\ldots (3.13)$$

3.2.2.2 Roe

Based on approximating the Euler Equation with linearization,

$$\mathbf{Q}_{\mathbf{j+1/2}} = \frac{\mathbf{1}}{\mathbf{2}}(\mathbf{F}_{\mathbf{j}}^{\mathbf{n}} + \mathbf{F}_{\mathbf{j+1}}^{\mathbf{n}}) - \frac{\mathbf{1}}{\mathbf{2}}\sum_{\mathbf{k=1}}^{\mathbf{3}}\left|\boldsymbol{\lambda}^{\mathbf{k}}\right|\boldsymbol{\alpha}^{\mathbf{k}}\mathbf{r}^{\mathbf{k}} \ldots\ldots\ldots (\mathbf{3.14})$$

$$\boldsymbol{\alpha}^{\mathbf{k}} = \left[\frac{\boldsymbol{\Delta p} - \hat{\mathbf{p}}\,\hat{\mathbf{c}}\,\boldsymbol{\Delta u}}{\mathbf{2}\,\hat{\mathbf{c}}^{\mathbf{2}}}\ ,\ \frac{\boldsymbol{\Delta p} - \hat{\mathbf{c}}^{\mathbf{2}}\,\boldsymbol{\Delta\rho}}{\hat{\mathbf{c}}^{\mathbf{2}}}, \frac{\boldsymbol{\Delta p} + \hat{\mathbf{p}}\,\hat{\mathbf{c}}\,\boldsymbol{\Delta u}}{\mathbf{2}\,\hat{\mathbf{c}}^{\mathbf{2}}}\right]$$

Where,

$$\boldsymbol{\Delta p} = \mathbf{p}_{\mathbf{j+1}} - \mathbf{p}_{\mathbf{j}}$$

$$\boldsymbol{\Delta u} = \mathbf{u}_{\mathbf{j+1}} - \mathbf{u}_{\mathbf{j}}$$

$$\boldsymbol{\Delta\rho} = \boldsymbol{\rho}_{\mathbf{j+1}} - \boldsymbol{\rho}_{\mathbf{j}}$$

And $\boldsymbol{r^k}$ are right eigenvectors,

$$\mathbf{r}^{\mathbf{1}} = \begin{bmatrix} \mathbf{1} \\ \hat{\mathbf{u}} - \hat{\mathbf{c}} \\ \hat{\mathbf{H}} - \hat{\mathbf{u}}\,\hat{\mathbf{c}} \end{bmatrix},$$

$$\mathbf{r}^{\mathbf{2}} = \begin{bmatrix} \mathbf{1} \\ \hat{\mathbf{u}} \\ \frac{\hat{\mathbf{u}}^{\mathbf{2}}}{\mathbf{2}} \end{bmatrix},$$

$$\mathbf{r}^{\mathbf{3}} = \begin{bmatrix} \mathbf{1} \\ \hat{\mathbf{u}} + \hat{\mathbf{c}} \\ \hat{\mathbf{H}} + \hat{\mathbf{u}}\,\hat{\mathbf{c}} \end{bmatrix}$$

And Roe-averages are defined as,

$\hat{\mathbf{p}} = \sqrt{\boldsymbol{\rho}_{\mathbf{R}}\boldsymbol{\rho}_{\mathbf{L}}}$,

$$\hat{\mathbf{u}} = \frac{\sqrt{\boldsymbol{\rho}_{\mathbf{L}}\mathbf{u}_{\mathbf{L}}} + \sqrt{\boldsymbol{\rho}_{\mathbf{R}}\mathbf{u}_{\mathbf{R}}}}{\sqrt{\boldsymbol{\rho}_{\mathbf{L}}} + \sqrt{\boldsymbol{\rho}_{\mathbf{R}}}} \ldots\ldots\ldots (\mathbf{3.15})$$

$$\hat{\mathbf{H}} = \frac{\sqrt{\boldsymbol{\rho}_{\mathbf{L}}}\mathbf{H}_{\mathbf{L}} + \sqrt{\boldsymbol{\rho}_{\mathbf{R}}}\mathbf{H}_{\mathbf{R}}}{\sqrt{\boldsymbol{\rho}_{\mathbf{L}}} + \sqrt{\boldsymbol{\rho}_{\mathbf{R}}}}$$

With the eigenvalues,

$$\boldsymbol{\lambda}^{\mathbf{1}} = \hat{\mathbf{u}} - \hat{\mathbf{c}} \ ,$$

$$\boldsymbol{\lambda}^{\mathbf{2}} = \hat{\mathbf{u}} \ ,$$

$$\boldsymbol{\lambda}^{\mathbf{3}} = \hat{\mathbf{u}} + \hat{\mathbf{c}}$$

3.2.2.3 Osher

Osher scheme is defined as:

$$\mathbf{Q}_i^{n+1} = \mathbf{Q}_i^n - \frac{\Delta t}{\Delta x}\left(\mathbf{F}_{i+1/2} - \mathbf{F}_{i-1/2}\right), \ \textbf{……(3.16)}$$

The numerical flux is written as,

$$\mathbf{F}_{i+1/2} = \frac{1}{2}\left(\mathbf{F}(\mathbf{Q}_R^n) + \mathbf{F}(\mathbf{Q}_L^n)\right) - \frac{1}{2}\int_{\mathbf{Q}_L}^{\mathbf{Q}_R} \left|\mathbf{A}(\mathbf{Q})\right| d\mathbf{Q}, \ \textbf{……(3.17)}$$

Where the Jacobian matrix $\mathbf{A}(\mathbf{Q})$ of the flux $\mathrm{F}(\mathbf{Q})$ is diagonalizable.

$$\mathbf{A}(\mathbf{Q}) = \mathbf{R}(\mathbf{Q})\boldsymbol{\Lambda}(\mathbf{Q})\mathbf{R}^{-1}(\mathbf{Q}),$$

Where,

$\mathbf{R}(\mathbf{Q})$: Right Eigenvector
$\boldsymbol{\Lambda}(\mathbf{Q})$: Diagonalized Eigenvalues

Where $\left|\mathbf{A}(\mathbf{Q})\right|$ is defined as,

$$\left|\mathbf{A}(\mathbf{Q})\right| = \mathbf{R}(\mathbf{Q})\left|\boldsymbol{\Lambda}(\mathbf{Q})\right|\mathbf{R}^{-1}(\mathbf{Q}),$$

Integral can be evaluated by,

$$\Psi(s;\mathbf{Q}_L,\mathbf{Q}_R)=\mathbf{Q}_L+s(\mathbf{Q}_R-\mathbf{Q}_L),\quad s\in[0,1].$$

Numerical Flux can be rewritten as,

$$\mathbf{F}_{i+1/2}=\frac{1}{2}\left(\mathbf{F}(\mathbf{Q}_R^n)+\mathbf{F}(\mathbf{Q}_L^n)\right)-\frac{1}{2}\left(\sum_{N}^{j=1}\omega_j\left|\mathbf{A}(\Psi(s_j;\mathbf{Q}_L,\mathbf{Q}_R))\right|\right)\Delta\mathbf{Q}\text{. }\textbf{……(3.18)}$$

3.2.2.4 AUSM

Flux vector F can be split into pressure and convective terms, [23]

$$F=\begin{bmatrix}\rho\\ \rho u\\ \rho H\end{bmatrix}u+\begin{bmatrix}0\\ p\\ 0\end{bmatrix}=F^c+\begin{bmatrix}0\\ p\\ 0\end{bmatrix}\text{……}\textbf{…(3.19)}$$

Convective terms are now considered as passive quantities by velocity u defined at the cell interface, whereas pressure flux is governed by the acoustic wave speeds. Thus, Liou and Steffen**,** suggested discretizing of both these terms separately,

$$F_{1/2}^c=u_{1/2}\begin{bmatrix}\rho\\ \rho u\\ \rho H\end{bmatrix}_{L/R}=M_{1/2}\begin{bmatrix}\rho a\\ \rho au\\ \rho aH\end{bmatrix}_{L/R}\quad\textbf{……(3.20)}$$

Defining contributions from both “left” and “right” states, as

$$M_{1/2}=M_L^+ + M_R^+\textbf{……(3.21)}$$

They used Van Leer splitting,

$$M^{\pm}=\begin{cases}\dfrac{1}{4}(M\pm1)^2,\ \text{if } |M|\le 1;\\ \dfrac{1}{2}(M\pm|M|),\ \text{otherwise}\end{cases}$$

Similarly, pressure terms is defined as

$$p_{1/2}=p_L^+ + p_R^+$$

Defining pressure splitting as,

$$p^{\pm} = \begin{cases} \frac{p}{2}(1 \pm M), \text{ if } |M| \le 1; \\ \frac{p}{2}\frac{(M \pm |M|)}{M}, \text{ otherwise} \end{cases}$$

3.2.3 Exact Solution

The solution are compared with exact solution for 1D Riemann problem as discussed in [24]

3.3 Results

Table 3:2, 3:3, and 3:4 represent the relative L1 norm error with respect to exact solution for N = 101, 601 and 1001 respectively for all the eight methods.

Table 3:2 Relative L1 norm for pressure and CFL = 0.95

	N = 101	**N = 601**	**N = 1001**
Lax Friedrich	0.607959	0.017169913	0.006157909
Lax Wendroff	0.618796	0.01747597	0.005405728
Richtmyer	0.618796	0.01747597	0.006299732
MacCormack	0.619823	0.017504975	0.006310188
Roe	0.424722	0.011994953	0.003436984
Osher	0.425155	0.012007182	0.004328345
Van Leer	0.425163	0.012007408	0.004328427
AUSM	0.423365	0.011956629	0.003206158

Table 3:3 Relative L1 norm for velocity and CFL = 0.95

	N = 101	N = 601	N = 1001
Lax Friedrich	0.931925	0.026319326	0.009439304
Lax Wendroff	0.748071	0.021126941	0.006535059
Richtmyer	0.748071	0.021126941	0.007615833
MacCormack	0.735065	0.020759627	0.007483424
Roe	0.431365	0.012182564	0.003490741
Osher	0.431159	0.012176746	0.00438947
Van Leer	0.432567	0.012216511	0.004403804
AUSM	0.430815	0.012167031	0.003262578

Table 3:4 Relative L1 norm for density and CFL = 0.95

	N = 101	N = 601	N = 1001
Lax Friedrich	0.508641	0.014364985	0.005151935
Lax Wendroff	0.497535	0.01405133	0.004346407
Richtmyer	0.497535	0.01405133	0.005065219
MacCormack	0.496427	0.014020038	0.005053939
Roe	0.385014	0.010873524	0.003115654
Osher	0.385028	0.01087392	0.003919827
Van Leer	0.385974	0.010900636	0.003929458
AUSM	0.385726	0.010893632	0.002921117

3.3.1 Finite Difference Method

3.3.1.1 Lax-Friedrich

Figure 3:1 shows numerical solution using Lax Friedrich scheme for grid resolution n = 601, and CFL number = 0.1 in comparison to Riemann solution. Figure 3:2 shows solution Lax Friedrich scheme for grid resolution n = 601, and CFL number = 0.95 in comparison to Riemann solution. Refining the grid size better captures the sharp

gradients. Hence, higher grid resolution was used to evaluate the effect of CFL. The plot for velocity is smoothed out with a parabolic shape in comparison to straight line of analytical solution. As the CFL number was decreased, more oscillations were apparent in velocity plot.

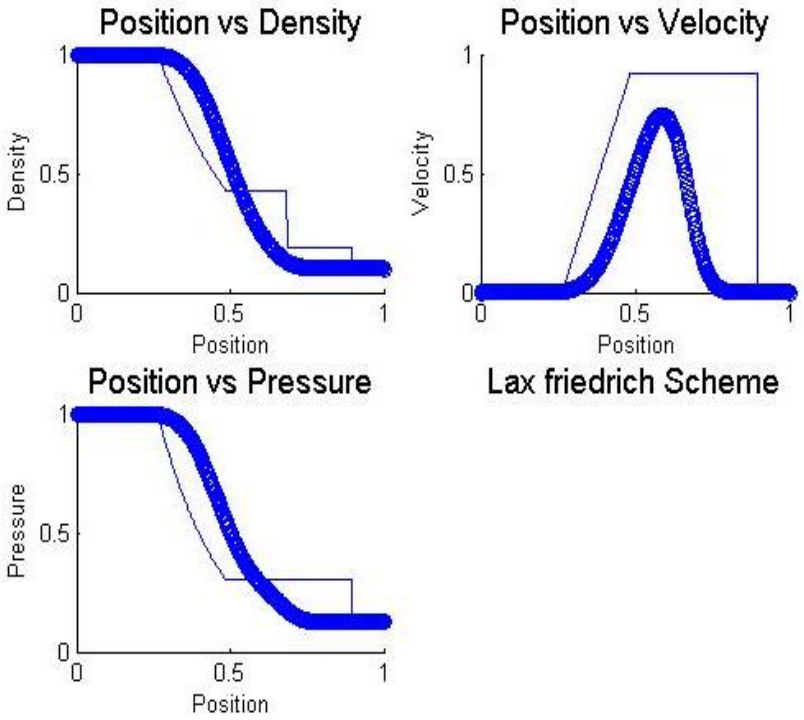

Figure 3:1 The Solutions by Lax-Friedrich's Scheme with CFL = 0.1

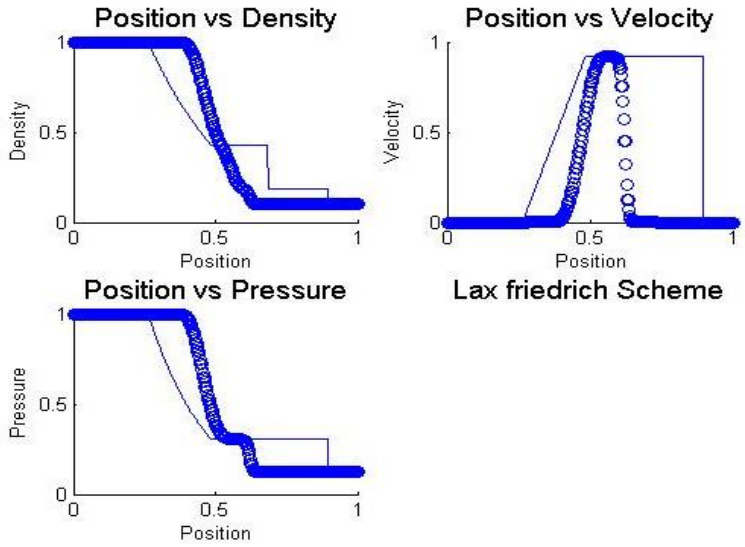

Figure 3:2 The Solutions by Lax-Friedrich's Scheme with CFL = 0.95

3.3.1.2 Lax-Wendroff

Figure 3:3 shows numerical solution using Lax-Wendroff scheme for grid resolution n = 601, and CFL number = 0.1 in comparison to Riemann solution. Figure 3:4 shows solution Lax-Wendroff scheme for grid resolution n =601, and CFL number = 0.95 in comparison to Riemann solution. The plot for velocity is smaller in comparison to straight line of analytical solution. Refining the grid size better captures the sharp gradients. Hence, higher grid resolution was used to evaluate the effect of CFL. As the CFL number was decreased, amplitude of oscillations increased at the discontinuity.

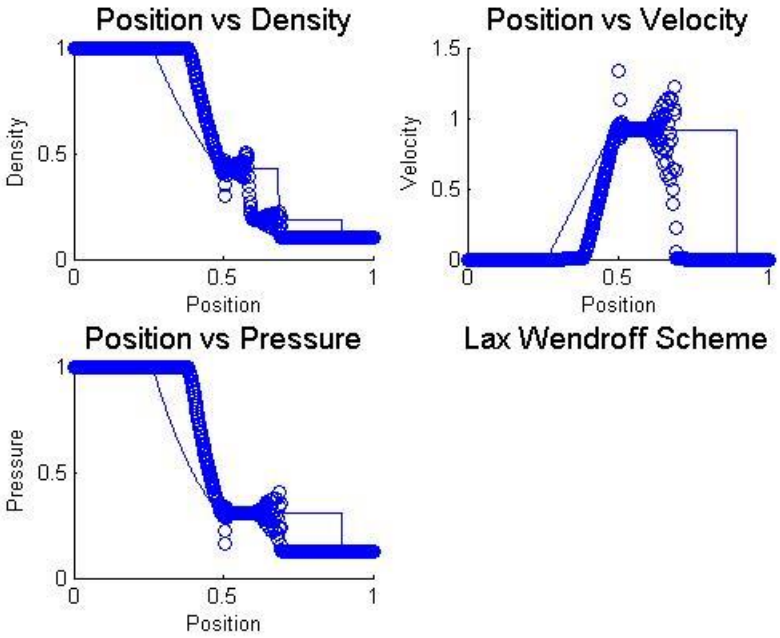

Figure 3:3 The Solutions by Lax Wendroff's Scheme with CFL = 0.1

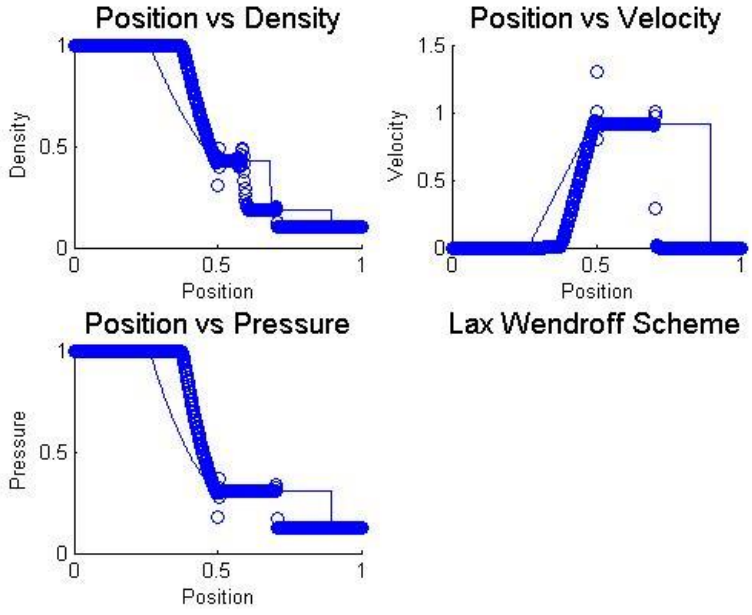

Figure 3:4 The Solutions by Lax Wendroff's Scheme with CFL = 0.95

3.3.1.3 MacCormack

Figure 3:5 shows numerical solution using MacCormack scheme for grid resolution n = 601, and CFL number = 0.1 in comparison to Riemann solution. Figure 3:6 shows solution MacCormack scheme for grid resolution n = 601, and CFL number = 0.95 in comparison to Riemann solution. Refining the grid size better captures the sharp gradients. Hence, higher grid resolution was used to evaluate the effect of CFL. As the CFL number was decreased, MacCormack scheme breaks down.

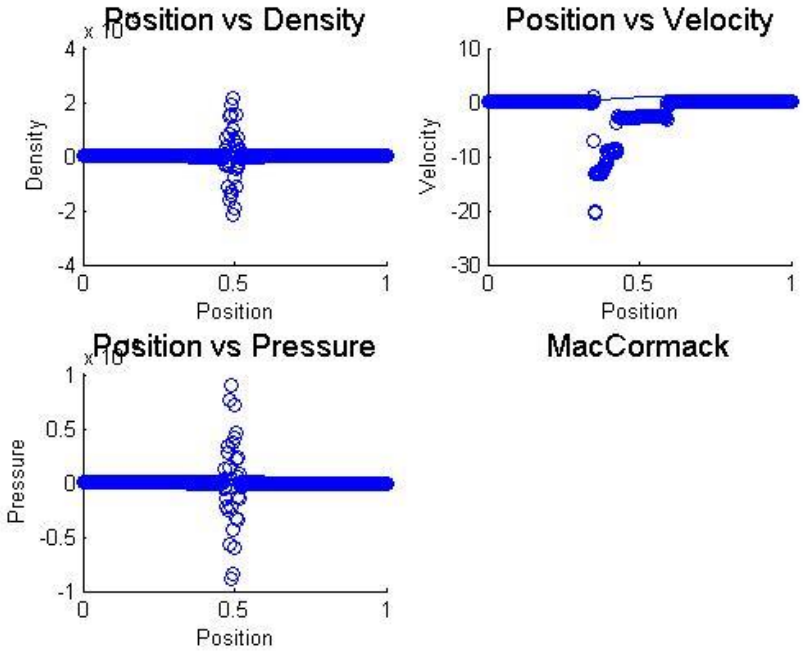

Figure 3:5 The Solutions by MacCormack Scheme with CFL = 0.1

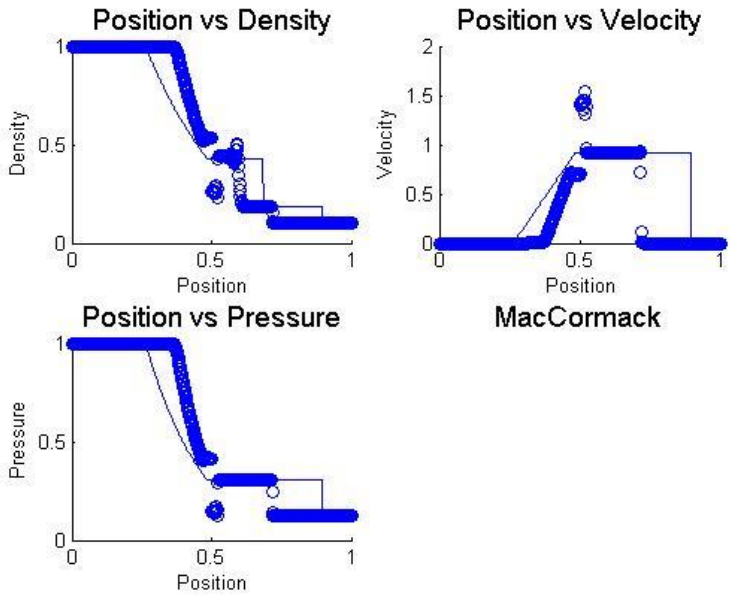

Figure 3:6 The solutions by MacCormack Scheme with CFL = 0.95

3.3.1.4 Richtmyer

Figure 3:7 shows numerical solution using Richtmyer scheme for grid resolution n = 601, and CFL number = 0.1 in comparison to Riemann solution. Figure 3:8 shows solution Richtmyer scheme for grid resolution n = 601, and CFL number = 0.95 in comparison to Riemann solution. Refining the grid size better captures the sharp gradients. Hence, higher grid resolution was used to evaluate the effect of CFL. It shows oscillatory behavior but does not break down.

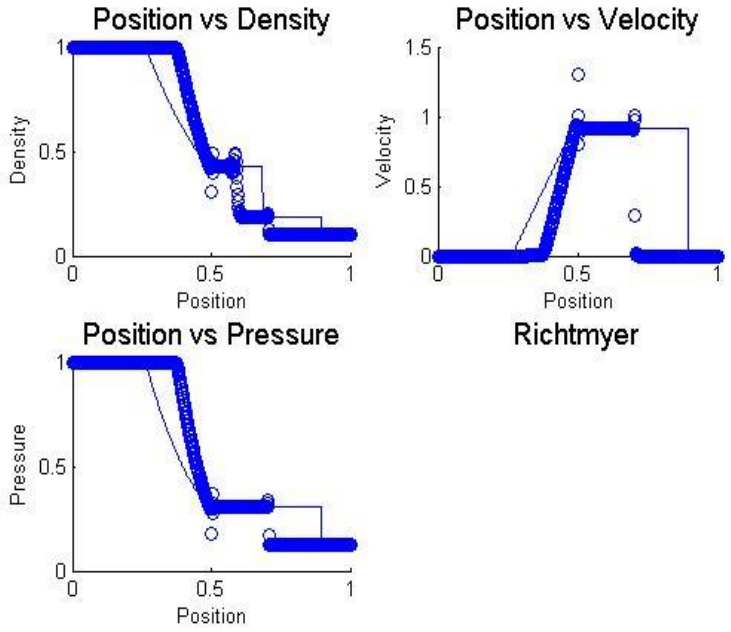

Figure 3:7 The Solutions by Richtmyer Scheme with CFL = 0.1

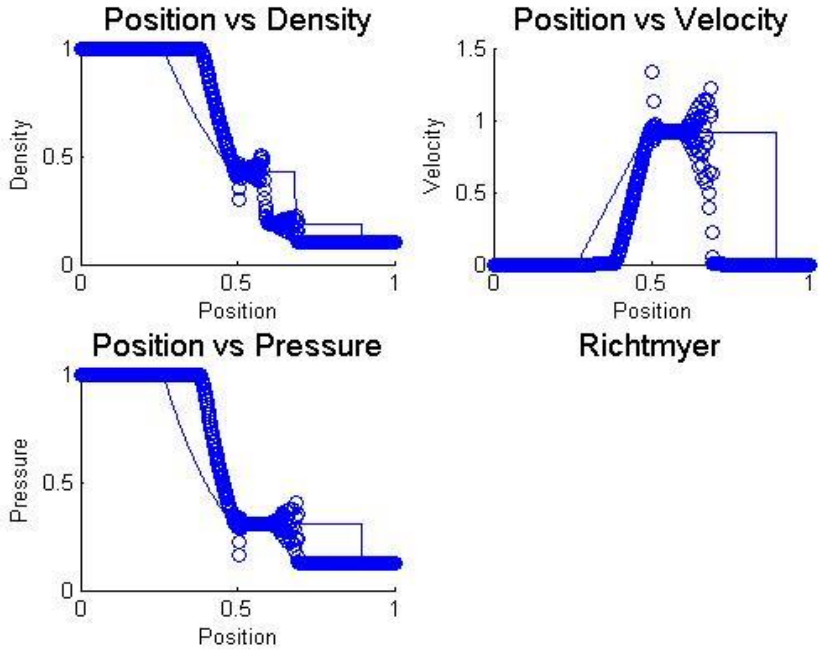

Figure 3:8 The Solutions by Richtmyer Scheme with CFL = 0.95

3.3.2 Finite Volume Method

3.3.2.1 Van Leer

Figure 3:9 shows numerical solution using Van Leer scheme for grid resolution n = 601, and CFL number = 0.1 in comparison to Riemann solution. Figure 3:10 shows solution Van Leer scheme for grid resolution n = 601, and CFL number = 0.95 in comparison to Riemann solution. Refining the grid size better captures the sharp gradients. Hence, higher grid resolution was used to evaluate the effect of CFL. Changing CFL number does not produce any appreciable effect on the solution. It provides an improvement over solution from finite difference methods.

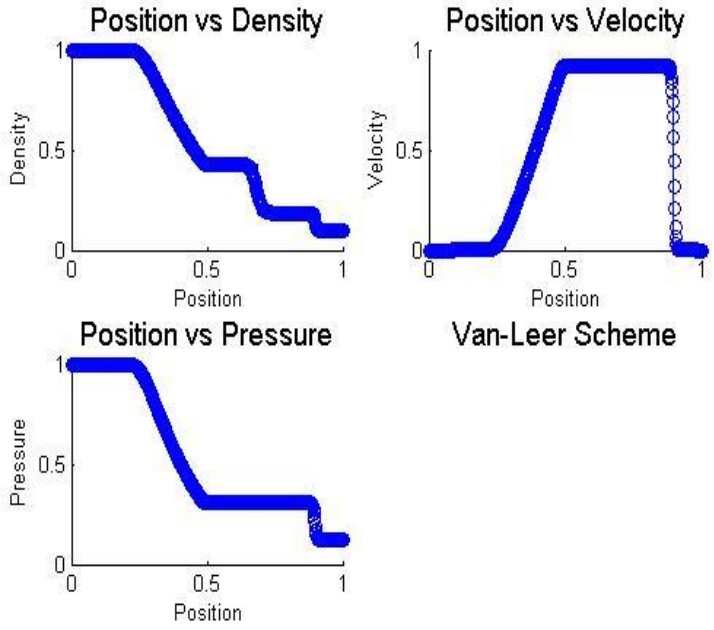

Figure 3:9 The Solutions by Van Leer Scheme with CFL = 0.1

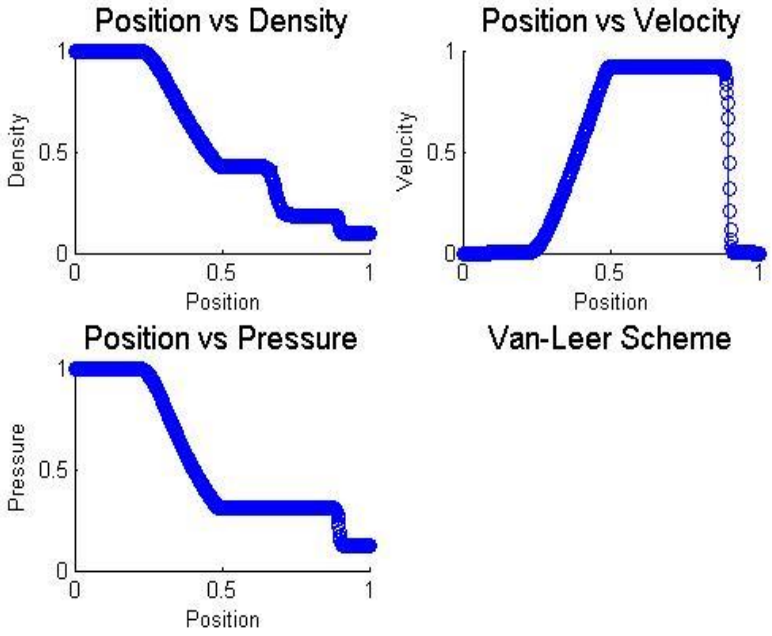

Figure 3:10 The Solutions by Van Leer Scheme with CFL = 0.95

The Solution graphs for following schemes can be seen in Appendix A.

3.3.2.2 Roe

Refining the grid size better captures the sharp gradients. Hence, higher grid resolution was used to evaluate the effect of CFL. Changing CFL number does not produce any appreciable effect on the solution. It provides an improvement over solution from finite difference methods. It is easier to implement in comparison to Van Leer scheme.

3.3.2.3 Osher

Refining the grid size better captures the sharp gradients. Hence, higher grid resolution was used to evaluate the effect of CFL. It provides an improvement over solution from finite difference methods.

3.3.2.4 AUSM

Refining the grid size better captures the sharp gradients. Hence, higher grid resolution was used to evaluate the effect of CFL. It provides an improvement over solution from finite difference methods.

3.3.3 Absolute Error Plots

Figure 3:11, 3:12, 3:13, 3:14, 3:15, and 3:16 represent the absolute error for the schemes.

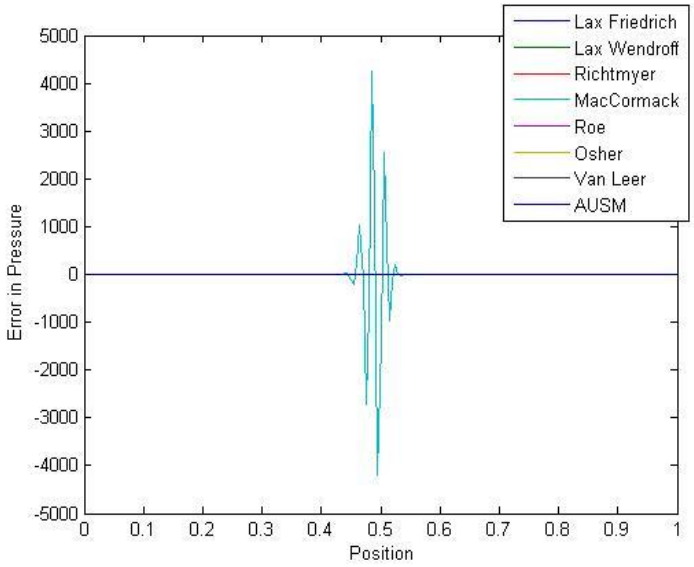

Figure 3:11 Absolute Error in Pressure vs Position for N = 601 and CFL = 0.1

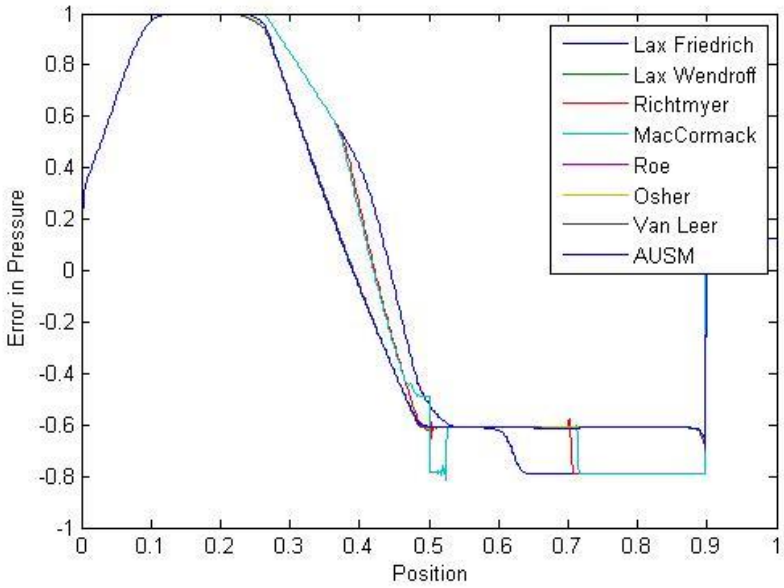

Figure 3:12 Absolute Error in Pressure vs Position for N = 601 and CFL = 0.95

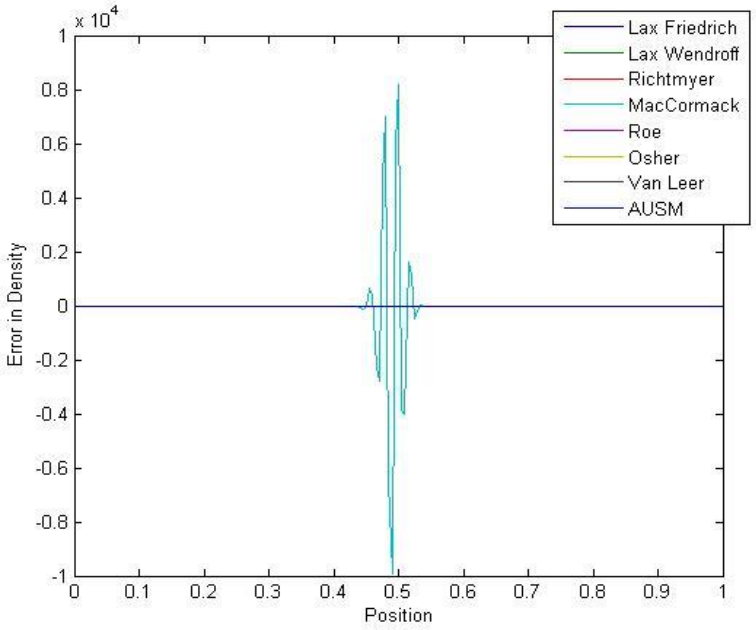

Figure 3:13 Absolute Error in Density vs Position for N = 601 and CFL = 0.1

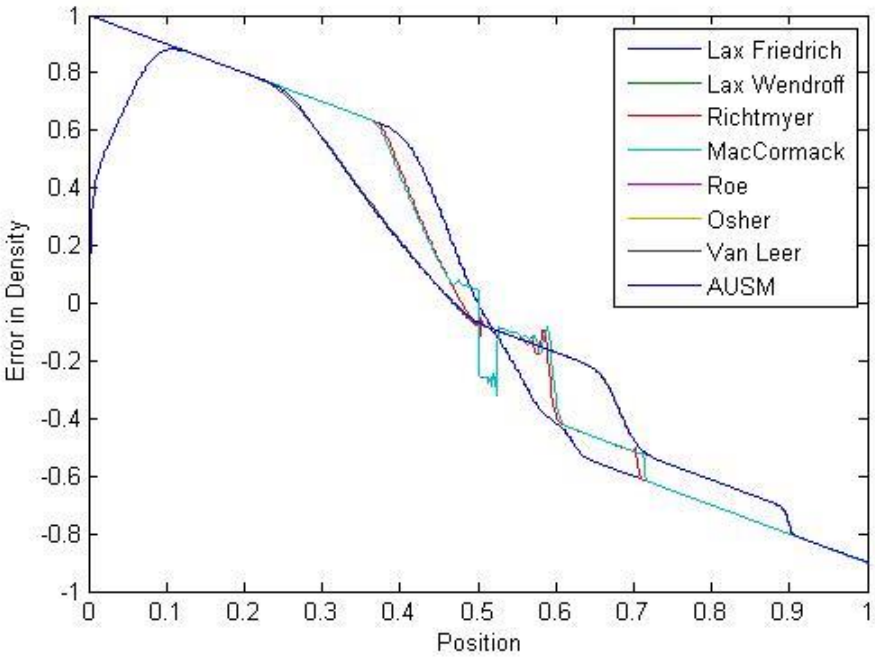

Figure 3:14 Absolute Error in Density vs Position for N = 601 and CFL = 0.95

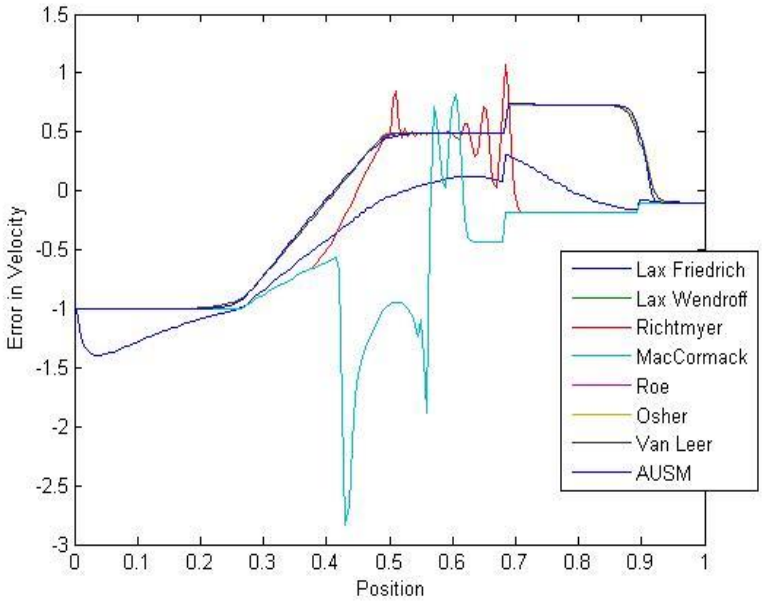

Figure 3:15 Absolute Error in Velocity vs Position for N = 601 and CFL = 0.1

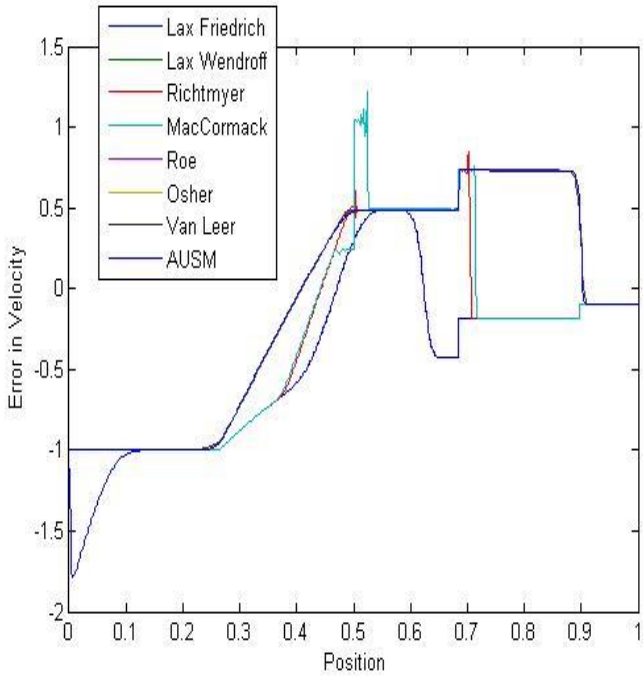

Figure 3:16 Absolute Error in Velocity vs Position for N = 601 and CFL = 0.95

Summary of effect of varying grid resolution, CFL, and run time for various numerical schemes to solve 1D Euler Equations is presented in Table 3:5. Run time will vary based on the computer processor.

Table 3:5 Summary of effect of varying grid resolution, CFL, and run time for various numerical schemes to solve 1D Euler equations

	Grid Resolution (n = 101; 601; 1001)	**CFL Number (= 0.1; 0.95) at n =601**	**Run time (in seconds)**
Lax-Friedrich	Refining Grid Size enables better capture of steep gradients of the solution	More oscillations observed when CFL number is decreased. More apparent in velocity plot	0.029939
Lax-Wendroff	Refining Grid Size enables better capture of steep gradients of the solution	Amplitude of oscillation decreased at the discontinuity decreased as CFL number was increased	0.038803
Richtmyer	Refining Grid Size enables better capture of steep gradients of the solution	Amplitude of oscillation decreased at the discontinuity decreased as CFL number was increased	0.038794
MacCormack	Refining Grid Size enables better capture of steep gradients of the solution	Breaks down as CFL number decreases	0.038952
Roe	Refining Grid Size enables better capture of steep gradients of the solution	Less than 1% change in CFL condition	1.05221
Van Leer	Refining Grid Size enables better capture of steep gradients of the solution	Less than 1% change in CFL condition	3.533449
Osher	Refining Grid Size enables better capture of steep gradients of the solution	Less than 1% change in CFL condition	5.353352
AUSM	Refining Grid Size enables better capture of steep gradients of the solution	Less than 1% change in CFL condition	5.407929

3.4 Discussion

The objective of this study was to review the most commonly used numerical schemes for solving one-dimensional compressible, unsteady Euler equations for a perfect gas. We compared Lax-Friedrich, Lax-Wendroff, Richtmyer, MacCormack, Roe,

Van Leer, Osher, and AUSM schemes in terms of accuracy, resolving shock and contact discontinuity, ease in code implementation, and efficiency.

Comparing relative L1 norm errors for pressure, velocity, and density at N = 101, 601, and 1001, it is evident that all the schemes have lower error as the grid resolution increases. L1 norm errors were not significantly different for N=601 in comparison to N=100. Also, N=601 captured the gradients in the solution. Grid resolution of 601 points was picked to evaluate the CFL number, since it was considered sufficient for capturing shock and contact discontinuity while being computational more efficient than 1001 grid points.

Appendix A consists of absolute error plots comparing solution for pressure, velocity and density for CFL number =0.1 and 0.95 at N =601. There are minor differences between the finite volume schemes for the two CFL number. For finite difference scheme, there are spurious oscillations pressure error plot caused by MacCormack scheme. The solution becomes significantly better when CFL number is increased to 0.95.

Lax-Friedrich, Lax-Wendroff, Richtmyer, and MacCormack scheme suffer from dispersion, and spurious oscillations. Even though, Lax-Wendroff scheme is much better than the Lax-Friedrichs method at resolving the shock, the method being dispersive produces large oscillations near the discontinuity. In addition, these methods fail to resolve the contact discontinuities accurately. MacCormack method solution fails for CFL number < 0.6.

Roe, Van Leer, Osher, and AUSM schemes are more stable than finite difference methods discussed earlier. Even though these schemes have a higher run time, they resolve shock and contact discontinuities more accurately. Hence, Finite volume methods are a better choice for solving Euler equations. Only minor differences are present in solution calculated using these four methods.

All these schemes were evaluated based on four aspects: its accuracy in comparison to exact solution, its ability to capture shock, the computation speed and the complexity of the implementation. Lax-Friedrich, Lax-Wendroff, Richtmyer, and MacCormack scheme are computationally efficient as well as easy to implement. However, these methods do not resolve shock very well. Roe, Van Leer, Osher, and AUSM provide robust solution with improved accuracy for efficiently resolving shocks. However, Van Leer and Osher are present a complex challenge for implementation. Roe and AUSM scheme are algorithmically simpler, which implies it easier to translate them into computer codes. Hence, Roe and AUSM scheme are practical choice for solving Euler 1D. The assumption for analytical solution involve isentropic and these equations don't consider influence of geometry as in 2D cases.

CHAPTER IV

TWO DIMENSIONAL SHOCK TUBE

This Chapter discusses development of 2D computational model to simulate the shock wave propagation in our shock tube, and presents a comparison between fully-ruptured membrane model with half-ruptured membrane model.

4.1 Introduction

4.1.1 Objective

Consistency and reliability in the data is of utmost priority for gaining better understanding of bTBI. CFD models can be used for shock tube design iteration to obtain data consistent with blast profiles of military ordnance. However, it is necessary to develop a reliable CFD model beforehand. Hence, 2D computational model to simulate the shock wave propagation in our shock tube were developed.

4.1.2 Governing Equations

According to literature [25, 26], we concluded that 2D axisymmetric model is the most appropriate representation of a cylindrical shock tube.

Continuity Equation for 2D axisymmetric model is as follows:

$$\frac{\partial \rho}{\partial t} + \frac{\partial (\rho v_x)}{\partial x} + \frac{\partial (\rho v_r)}{\partial r} + \frac{\rho v_r}{r} = 0 \ldots\ldots\ldots (4.1)$$

The conservative form of Euler Equation for unsteady, non-reactive perfect gas is as follows:

$$\frac{\partial}{\partial t}\begin{bmatrix}\rho\\ \rho v_x\\ \rho v_r\\ \rho E\end{bmatrix}+\frac{\partial}{\partial x}\begin{bmatrix}\rho v_x\\ \rho v_x v_x+P\\ \rho v_x v_r\\ (\rho E+P)v_r\end{bmatrix}+\frac{\partial}{\partial r}\begin{bmatrix}\rho v_r\\ \rho v_x v_r\\ \rho v_r v_r+P\\ (\rho E+P)v_r\end{bmatrix}+\frac{1}{r}\begin{bmatrix}\rho v_r\\ \rho v_x v_r\\ \rho v_r v_r\\ (\rho E+P)v_r\end{bmatrix}=0 \ldots\ldots (4.2)$$

Equation of State for perfect gas,

$$E=\frac{P}{\gamma-1}+\frac{1}{2}\rho(v_x^2+v_r^2) \ldots\ldots\ldots\ldots (4.3)$$

Where,

$\rho = Density$

$v = Velocity$

$p = Pressure$

$E = Total\ Energy\ per\ unit\ mass\ of\ the\ fluid$

4.2 Method

4.2.1 Computational Domain

Figure 4:1 represents the entire geometry of the Robbins-Moreno shock tube. The computational domain was based on this shock tube. The internal diameter of the tube (d) was 12 inches. The length of driver section was 1.5 ft. Three different lengths for the driven section (L_d): 10ft, 15ft, and 20ft were used.

The blast wave profiles in a tube for two different geometries, which model the membrane in different ways, were compared. Figure 4:2 is a 2D geometric representation of shock tube that depicts instantaneous and full rupture of the membrane.

Figure 4:3 represents computational model for fully-ruptured shock tube model. Figure 4:4 is a 2D geometric representation of shock tube that depicts instantaneous but only half rupture of the membrane. These geometric representations were created in Solidworks (Dassault Systemes SolidWorks Corp, Waltham ,MA). By setting bottom wall as a symmetry plan, only half of the geometry was modeled. Figure 4:5 represent the computational domain for half-ruptured shock tube model.

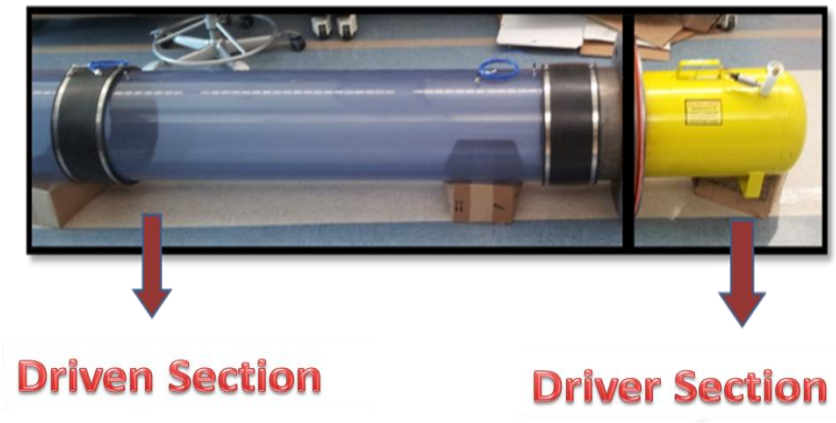

Figure 4:1 Shock Tube Built in Biomechanical Environment Lab

Figure 4:2 Geometric Model of the Shock Tube Representing Fully-ruptured Membrane

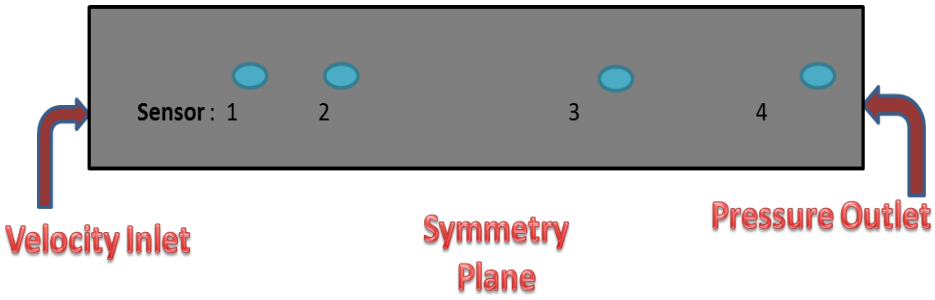

Figure 4:3 Computational Domain for Shock Tube Model, Representing Fully-ruptured Membrane, with the Boundary Conditions and Location of Sensors

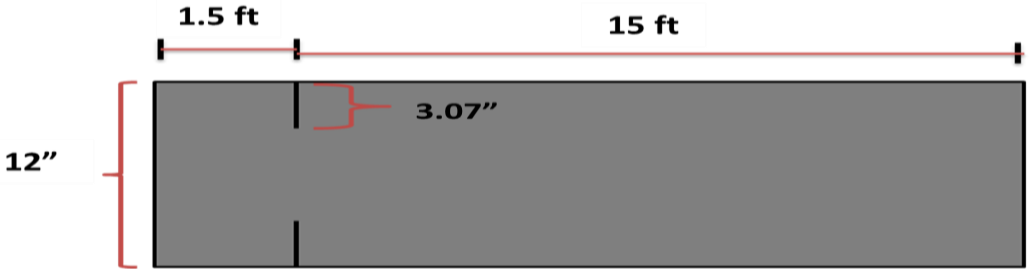

Figure 4:4 Geometric Model of the Shock Tube Representing a Half-ruptured Membrane

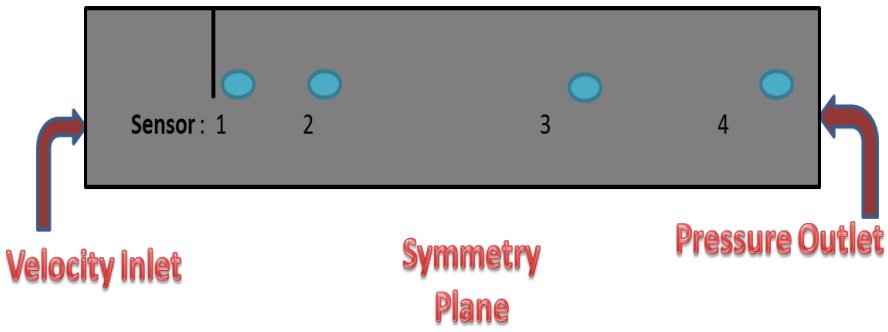

Figure 4:5 Computational Domain for Shock Tube Model, Representing Half-ruptured Membrane, with the Boundary Conditions and Location of Sensors

At the outlet, zero-pressure boundary condition was set. No-slip boundary condition was imposed on the top wall and the half-ruptured membrane. Pressure data was obtained from locations marked as sensor 1, 2, 3, 4 that correspond to the position of pressure sensor probes as placed in the Robbins-Moreno shock tube. The location for sensor for different lengths of driver section is summarized in Table 4:1. These distances were measured from the inlet. Hence, they include the driver section length. Sensor 4 corresponds to the location of where the animal will be placed in shock tube. Hence, we are most interested in pressure profiles at this location.

Table 4:2 summarizes the simulation parameters for both the models. For both these computational domain, inviscid model was compared to viscous model. For viscous model, k-ε turbulence model was used.

Table 4:1 Location of points corresponding to the sensors in the shock tube from where data was obtained

Driven Section 10 ft.	
	distance from inlet (ft.)
Sensor 1	2.26
Sensor 2	5.68
Sensor 3	9.19
Sensor 4	10.23
Driven Section 15 ft.	
Sensor 1	2.26
Sensor 2	5.68
Sensor 3	14.06
Sensor 4	15.99
Driven Section 20 ft.	
Sensor 1	2.26
Sensor 2	5.68
Sensor 3	14.06
Sensor 4	20.93

Table 4:2 Simulations parameters for fully-ruptured and half-ruptured membrane model

	Left Domain	**Right Domain**
Pressure, p [psi]	Variable	14.7
Density, ρ [kg/m^{3}]	Variable	2.46
Velocity, u [m/s^{2}]	0	0
Gamma	1.4 for air	

4.2.2 Numerical Discretization

Commercial software Star CCM+ (CD-adapco., NY, USA) was used. AUSM finite volume discretization was implemented to accurately capture shock and contact discontinuities for both fully-ruptured membrane model and half-ruptured membrane model. Second-order implicit scheme was used for temporal discretization. MATLAB was used for post-processing of the data. We made use of TAMU supercomputing

facility that is equipped with Compute nodes, which have two processors each; a Xeon 5680 series 3.33GHz hex-core processor with a 12MB unified L3 cache. Peak performance for the 12 cores is 160 GFLOPS.

As a test case for establishing spatial and temporal convergence, computational domain with 15 ft. driven section was used. Initial pressure for driver section was 37.5psi and driven section was 14.7psi. Air was the working fluid. Pressure profiles were compared for grid independence.

The spatial convergence of the mesh was examined using half-ruptured membrane model. The method involved using five successively finer grids. Since the exact solution is unknown, "Very Fine" mesh was used as the exact solution to calculate the error. As the grid is refined, the spatial discretization error should asymptotically approach zero. The grid statistics are summarized in Table 4:3.

Table 4:3 Grid Statistics

Grid	Number of Cells	Number of Faces	Number of Vertices
Very Coarse	1925	8717	9025
Coarse	15871	76091	78141
Medium	77242	386948	389610
Fine	320024	1607890	160600
Very Fine	1269598	6365989	6344200

For examining temporal Convergence, since the exact solution is unknown, time step of 1e-6 s at t= 0.016 s was used for sake of error estimation, which were plotted against normalized time step (normalized with the largest time step) for second order scheme.

4.2.3 Statistical Analysis

Computational data from the four models: inviscid fully-ruptured membrane, viscous fully-ruptured membrane, inviscid half-ruptured membrane, and the viscous half-ruptured membrane was compared to the experimentally obtained data. RMS error was calculated with $\hat{y}_i$ as the computational values and y_i as the experimental values:

$$\text{RMS error} = \sqrt{\frac{\sum_{i=1}^{n} (\hat{y}_i - y_i)^2}{n}}$$

4.3 Result

Table 4:4 shows the five consecutively finer meshes that were used. Very fine mesh was used as the exact solution. Since, we are most interested in pressure vs. time data, pressure profiles were compared for establishing grid independence. Relative error was calculated for different meshes for pressure at sensor 4 data over 15ms time. Relative error increases as the mesh becomes coarser. For computations here on, medium refined grid was used to achieve accuracy while staying computationally efficient. Table 4:5 is the temporal discretization error plot as a function of time step. Relative error was calculated for different meshes for pressure. Time step of 1e-6 s was used as the exact solution. Relative error for sensor 4 data was calculated. It increased as the time step becomes larger. For computations following, time step of 1e-5 s was used to achieve accuracy while staying computationally efficient

Table 4:4 Spatial Convergence - Grid Statistics

Grid	Number of	Number of	Number of Vertices	Relative
Very	1925	8717	9025	3.7479e4
Coarse	15871	76091	78141	2.6237e2
Medium	77242	386948	389610	4.26351e-6
Fine	320024	1607890	160600	8.56739e-8
Very Fine	1269598	6365989	6344200	0

Table 4:5 Temporal errors for pressure calculated using different time steps

Time Step	Relative Error
1e-5	0.020087052
1e-4	0.216152238
5e-4	0.302205883

Figure 4:6 shows a comparison between pressure profiles for fully-ruptured versus half-ruptured membrane inviscid model with air as working fluid, and 37.5 psi burst pressure. Fully-ruptured membrane model showed a higher peak overpressure in comparison to half-ruptured model. There was a difference in rise time; fully-ruptured membrane model rises to peak overpressure earlier than half-ruptured model. In addition, the duration of negative overpressure was longer for fully-ruptured model.

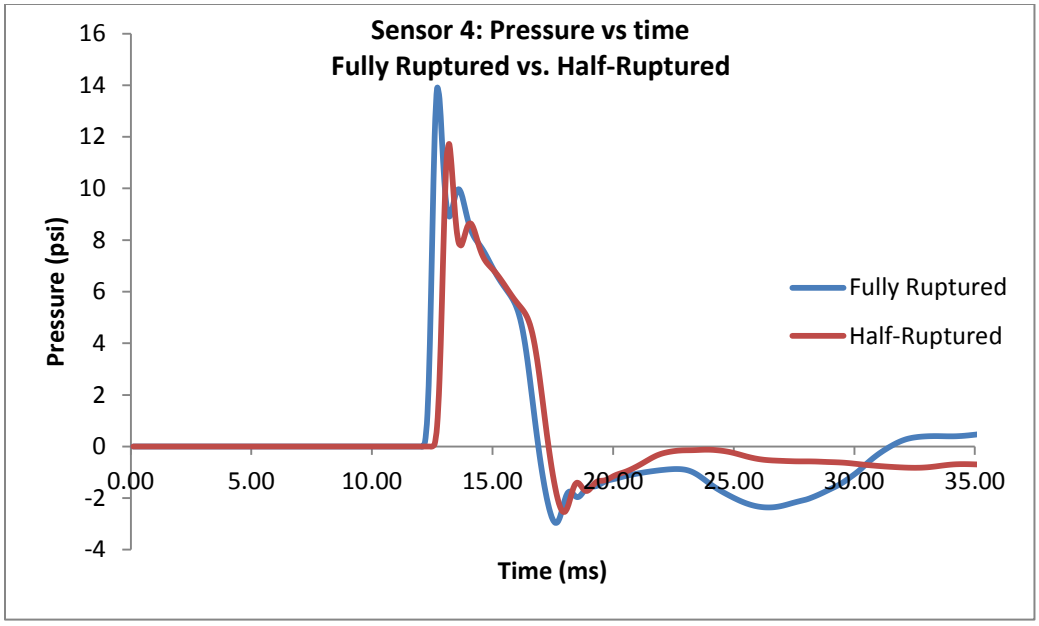

Figure 4:6 Pressure Profiles for Fully-ruptured Membrane and Half-ruptured Membrane Model

Figure 4:7, Figure 4:8, and Figure 4:9 shows the comparison between computational and experimental data for peak overpressure versus burst pressure in psi, for half-ruptured inviscid model at 10ft, 15ft, and 20 ft respectively. An example of comparison of pressure profile between experimental and computational, with burst pressure as 37.5psi and air as working fluid, is presented in Appendix B, Figure B:3

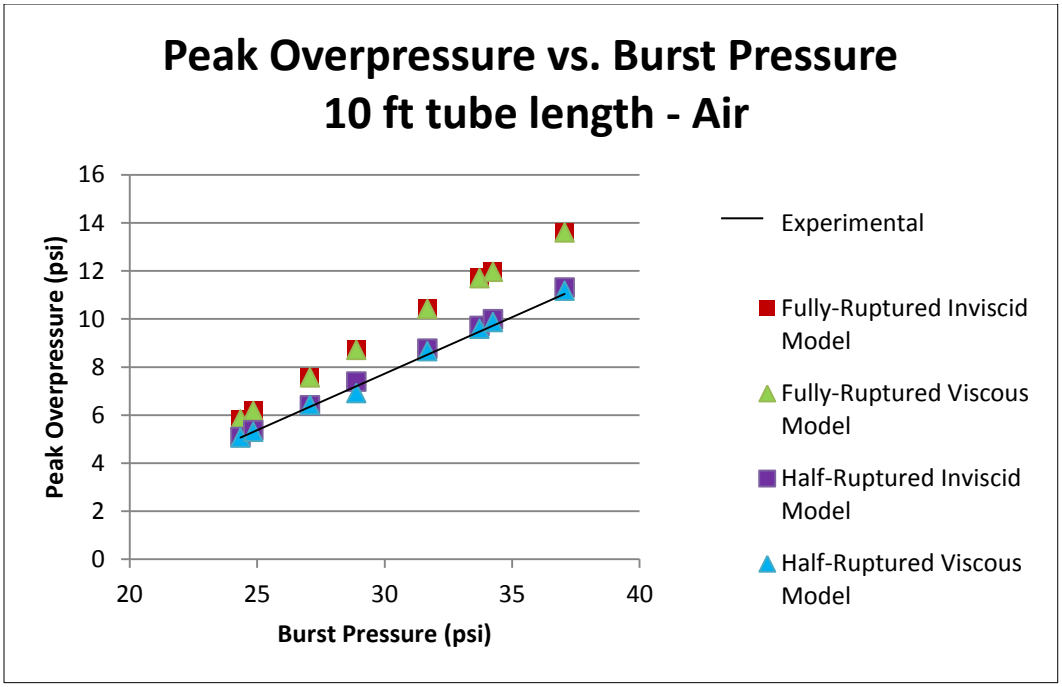

Figure 4:7 Comparison of Computational Peak Overpressure Versus Burst Pressure for 10 ft. Driver Section

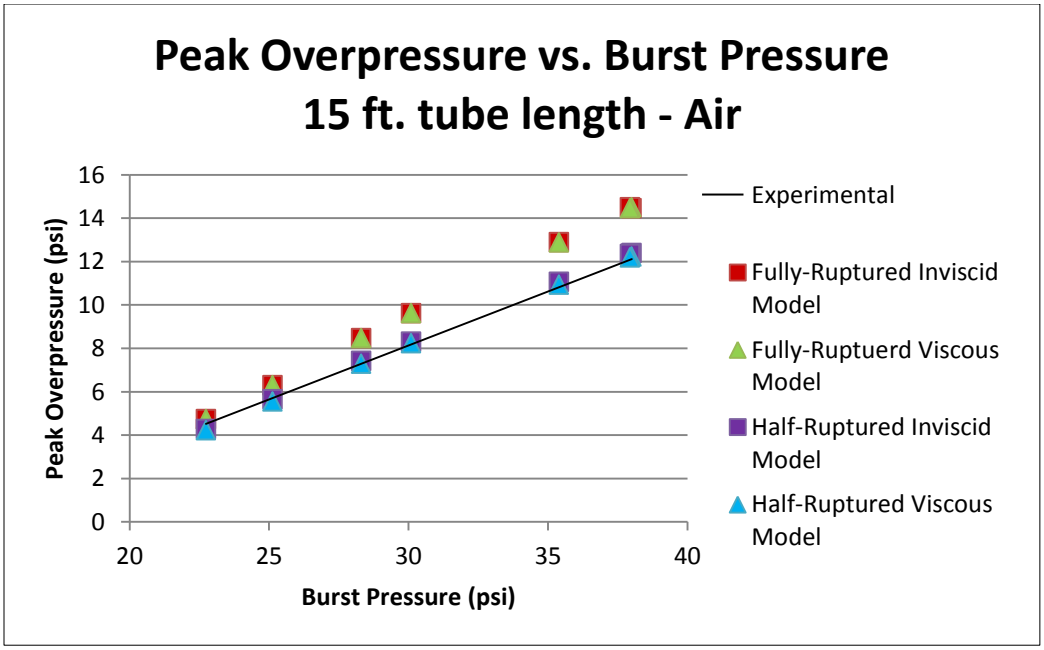

Figure 4:8 Comparison of Computational Peak Overpressure Versus Burst Pressure for 15 ft. Driver Section

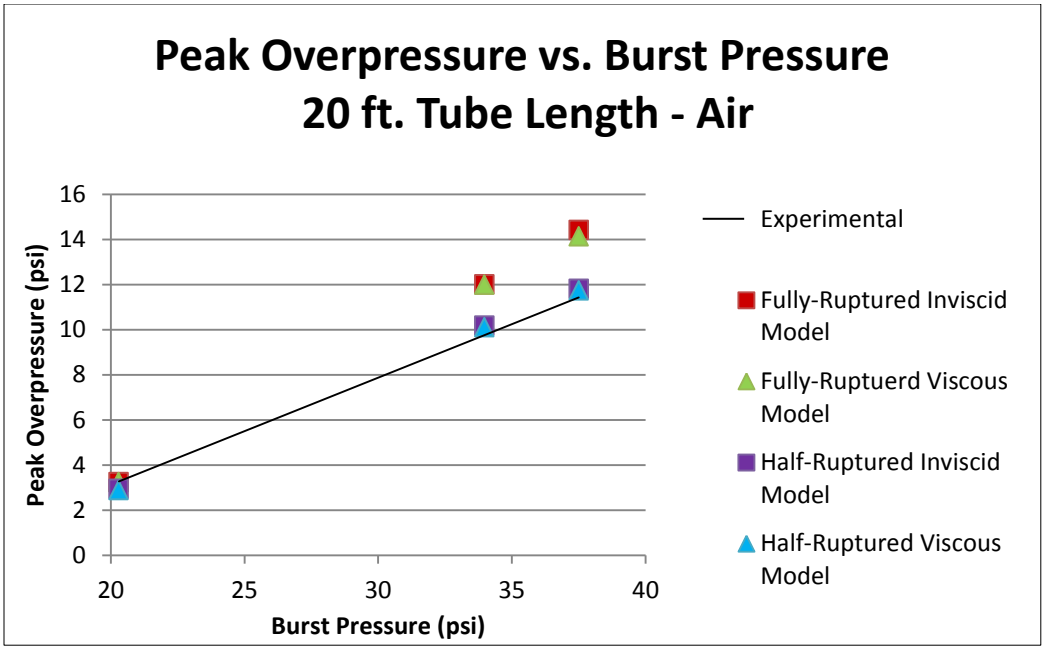

Figure 4:9 Comparison of Computational Peak Overpressure Versus Burst Pressure for 20 ft. Driver Section

Table 4:6 contains the summary of computational and experimental peak overpressure versus burst pressure in psi for all the four models as well as three different driven section length: 10ft, 15ft, and 20ft. It was found that rms error in peak overpressure for inviscid fully-ruptured model was ±1.78068 psi different than the experimental data for 10 ft. tube length. For 15 ft. tube length, the rms error was ±1.69737 psi. For, 20 ft. tube length, the rms error changed to ±2.39073 psi. It was found that rms error in peak overpressure for inviscid fully-ruptured model was ±1.7788 psi different from the experimental data for 10 ft tube length. For 15 ft. tube length, the rms error was ±1.69917 psi. For, 20 ft. tube length, the rms error changed to ±2.2322 psi. It was found that rms error in peak pressure for inviscid half-ruptured model was ±0.2781 psi different from the experimental data for 10 ft. tube length. For 15 ft. tube length, the rms error is ±0.4076 psi. For, 20 ft. tube length, the rms error changed to ±0.97922 psi. It was found that rms error in peak pressure for inviscid fully-ruptured model was ±0.2729 psi different from the experimental data for 10 ft. tube length. For 15 ft. tube length, the rms error was ±0.38827 psi. For, 20 ft. tube length, the rms error changed to ±0.96694 psi.

Table 4:6 Summary of peak overpressure vs. burst pressure for the four models, and the related RMS errors of the peak overpressure.

Tube Length		Overpressure (psi)				
		Experimental	Computational (No Membrane)	Computational (Viscous - No Membrane)	Computational (Half Rupture)	Computational (Viscous - Half Rupture)
10 ft.	24.35	5.19	5.83	5.82	5.09	5.06
	24.86	5.35	6.17	6.16	5.36	5.3
	27.08	5.99	7.56	7.56	6.4	6.421
	28.9	7.25	8.71	8.71	7.39	6.91
	31.68	8.44	10.42	10.41	8.76	8.65
	33.73	9.6	11.7	11.69	9.7	9.58
	34.26	10.12	11.95	11.95	9.99	9.87
	37.06	10.76	13.59	13.6	11.3	11.17
RMS error			**1.78068**	**1.7788**	**0.2781**	**0.27292**
15 ft.	22.74	4.34	4.73	4.73	4.28	4.21
	25.13	5.81	6.3	6.3	5.65	5.55
	28.3	7.576	8.46	8.46	7.413	7.29
	30.09	8.1	9.62	9.62	8.3	8.23
	35.4	10.62	12.89	12.87	11.06	10.93
	38	11.55	14.46	14.5	12.39	12.23
	37.94	12.75	14.5	14.45	12.34	12.19
RMS error			**1.69737**	**1.69617**	**0.40762**	**0.38827**
20 ft.	20.3	3	3.24	3.24	2.94	2.88
	33.97	11.08	12.001	11.99	10.17	10.11
	37.5	10.38	14.41	14.13	11.81	11.74
RMS error			**2.39073**	**2.2322**	**0.97922**	**0.96694**

4.4 Discussion

The objective of this research was to develop a 2D computational model to simulate the shock wave propagation in our shock tube and validate the CFD model. 2D models were used instead of 1D to study the influence of membrane on the peak overpressure. Also, implication of variation in geometry of driven section which includes coupler were studied.

As the membrane between the two section ruptures, high pressure gas comes in contact with low pressure gas. This causes the velocity to change, which initiates the shock wave. Compression waves rapidly combine to form the shock front that travels at high speed down the shock tube. The expansion waves travel to opposite side of the shock. As the expansion waves eventually overtake the shock, it degrades the pressure. Rupture of the membrane in the shock tube is a key element in generation of a shock wave. The membrane rupture process is a non-conservative process [27]. Most of the shock tube models assume instantaneous rupture of the membrane at time t = 0, and any effects due to membrane curvature are ignored. However, the membrane does not completely disappear after rupture. Brun et. al. and Rothkopf et. al. studied the effect of membrane's opening process and its effect on flow regime of the shock wave [28, 29]. The presence of membrane causes a gradual flow evolution in comparison to instantaneous rupture. It also reduces the shock strength, the speed of the shock wave, and distance of propagation distance [30]. Figure 4:10 is an image from experiments conducted at BMEL. As seen in the image, membrane does not completely disappear from the path of shock wave propagation after mechanical rupture. The membrane for

Robbins-Moreno shock tube ruptures very consistently. Hence, membrane was included in the model and blast wave profile in a tube for two different geometries was compared. One of the geometries assumed instantaneous rupture; whereas, the second geometry had a half-opened orifice. A 25% and 75% opening were also considered. Changing the size of the opening significantly changed the peak overpressure. Based on comparison with experimental data, half-ruptured simulation scenario is closer to reality. Viscous model for both these models was also compared to the inviscid model. Computational model was compared to experimental data for various burst pressure, and tube length.

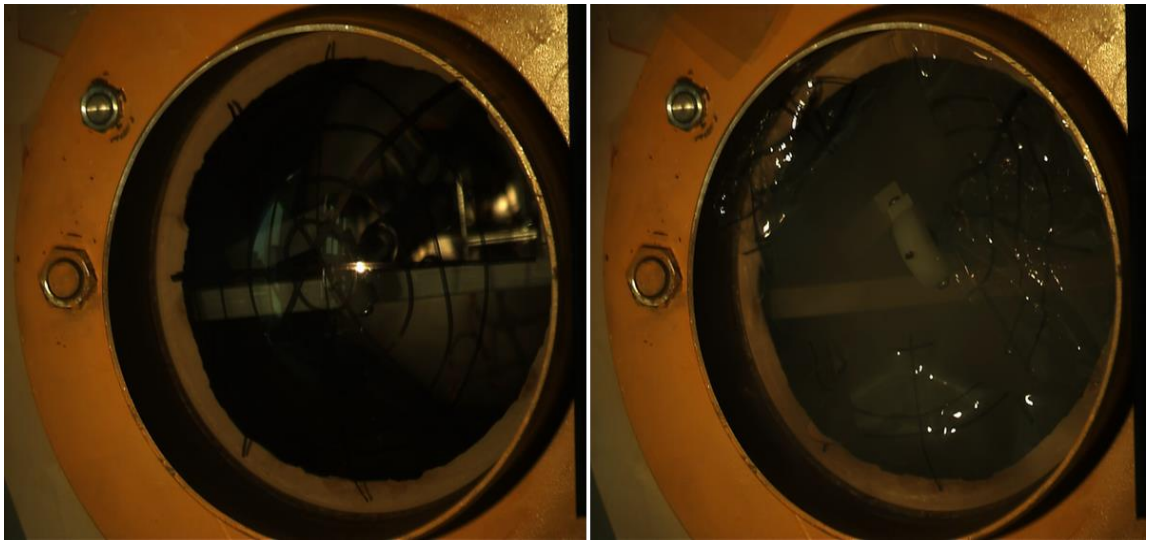

Figure 4:10 Membrane in Shock Tube (left) Before Mechanical Rupture, and (right) After Rupture

Difference of about 2 psi peak overpressure is significant, especially when testing small animal model. Since, this difference might cause more severe injury than intended. So, a fully-ruptured viscous model was tested to improve the accuracy of the 2D model.

The viscous model provided only a slight improvement. Hence, it was considered necessary to account for presence of membrane.

Accounting for presence of membrane provides a much accurate model to simulate a blast profile. Viscous half-ruptured model provides a slight improvement over the inviscid half-ruptured model. However, viscous models are computationally more expensive. Therefore, an inviscid half-ruptured membrane model was used in the following experiments.

As seen in appendix B, data was obtained from multiple points along the radius of the shock tube to establish that pressure profile is fairly insensitive to this location along cross-section. The distance corresponded to where the animal will be placed in during the experiments. The blast wave profile along the radius of the tube at the outlet was compared. It was observed that there was no difference in wave profiles near the outlet. Hence, the height of the probe will not affect the wave profile. However, the data was obtained from center of the tube, in order to achieve uniformity in location from which data is obtained; Since the following experiments use tubes with different diameter.

This study did not look at the effect of disappearance of membrane with time. However, considering the accuracy provided by inviscid half-ruptured model, it was deemed unnecessary to add the complexity transient membrane change. For purpose of our study, half-ruptured model replicates the experimental data quite accurately and efficiently.

Briefly, a computational model has been developed that can predict the strength of the shock wave produced by the shock tube to a high degree of accuracy. Following this

validation of our model, we can alter the shock tube parameters such as the geometry, working fluid, blast chamber to shock tube ratio etc., computationally in order to tune the shock tube system; such that the pressure profiles generated are better replications of the pressure profiles generated by military ordnance.

CHAPTER V

OPTIMIZATION OF SHOCK TUBE

This chapter discusses the optimization of our shock tube and development of empirical models that determine relationship between tube length, tube diameter, burst pressure, working fluid with the blast wave, specifically peak overpressure, positive phase duration, and positive impulse. The overall design and model is discussed.

5.1 Introduction

Finding an optimal physical design for a shock tube to obtain different blast profiles is extremely time-consuming and expensive. In addition, it is not well understood how various salient features of blast waves contribute to epidemiology of bTBI. Most research focuses solely on effect of exposure to various peak overpressure [7, 9, 31, 32].

However, there is variation in the peak overpressures, ranging between 5 to 30 psi, that are used to cause different degree of bTBI [6, 13, 33-36]. In addition to peak overpressure, the harmful effects of a blast wave may also depend on positive phase duration, negative phase duration and positive pressure duration. [37, 38] To be able to isolate and examine the effect of each of these features of blast waves, it is important to understand design factors that can be used to vary them.

Each shock tube configuration results in a pressure profile with distinct features. The principal goal of this study was to evaluate the effect of varying shock tube geometry, and working fluid on the four parameters of the resultant blast wave pressure

profile: peak overpressure, positive phase duration, positive phase impulse, negative phase magnitude, and develop empirical model to predict these key features.

5.2 Method

5.2.1 Computational Domain

Figure 5:1**,** Figure 5:2**,** Figure 5:3 are representations of 2D computational domain of shock tube for 8", 12", and 16" tube diameter respectively. Driver section remains 12" to replicate the experimental Robbins-Moreno shock tube. Hence, 8" and 16" diameter was chosen to emulate converging and diverging section respectively. The models were created in Solidworks (Dassault Systemes SolidWorks Corp, Waltham ,MA). By setting bottom wall as a symmetry plan, only half of the geometry was modeled. At the inlet, velocity inlet boundary condition was used with 0 m/s as the initial velocity. At the outlet, zero-pressure boundary condition was set at 14.7 psi. No-slip boundary condition was imposed on the top wall and the half-ruptured membrane. Data was obtained from open end, location that corresponds to the position of where the animal model will be placed in the Robbins-Moreno shock tube (Refer to Table C:1 in Appendix C for distances from inlet at which the data was obtained from for different tube lengths).

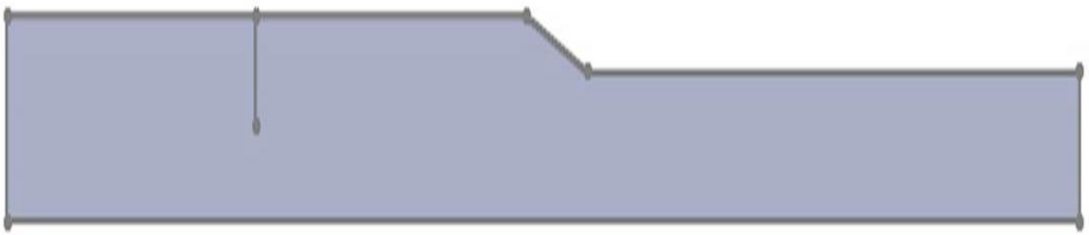

Figure 5:1 Shock Tube Model Representing a Half-ruptured Membrane for 8" Tube Diameter

Figure 5:2 Shock Tube Model Representing a Half-ruptured Membrane for 12" Tube Diameter

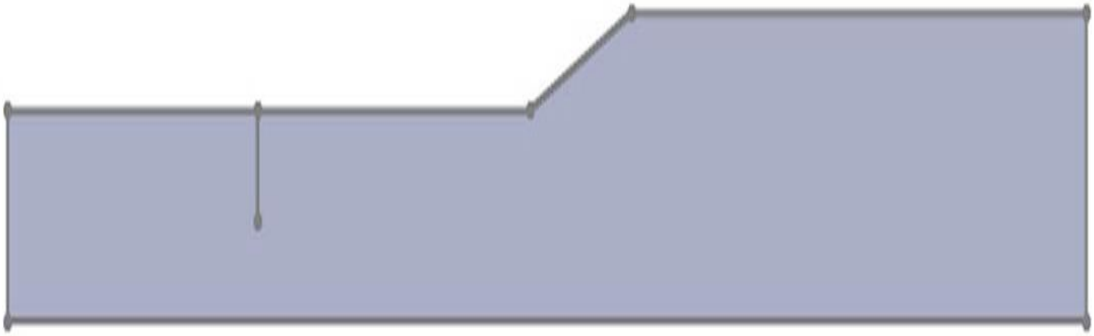

Figure 5:3 Shock Tube Model Representing a Half-ruptured Membrane for 16" Tube Diameter

5.2.2 Shock Tube Parameters

Table 5:1 shows the parameters that were used to characterize the pressure profile. 240 simulations were run to account for all the combinations of these parameters.

Table 5:1 Parameters used to characterize the pressure profile

Parameters	
Burst Pressure [psi]	[20, 25, 30, 35, 40, 45, 50, 55]
Working Fluid	[Air, He]
Tube Length [m]	[5, 10, 15, 20, 25]
Tube Diameter [inches]	[8, 12, 16]

5.2.3 Shock Tube Simulation

Commercial software Star CCM+ (CD-adapco., NY, USA). AUSM spatial discretization and second-order implicit temporal discretization (time step - 1e-5s) were implemented to accurately capture shock and contact discontinuities. The objective function on which design iteration will be based is pressure. MATLAB (Mathworks, Natick, Massachusetts, USA) was used for post-processing of the data. Positive impulse was calculated as the area under the overpressure-time curve for positive duration. TAMU supercomputing facility was used to run the simulations. It is equipped with Compute nodes, which have two processors each; a Xeon 5680 series 3.33GHz hex-core processor with a 12MB unified L3 cache. Peak performance for the 12 cores is 160 GFLOPS.

5.2.4 Statistical Tools to Obtain Empirical Models

Design of experiments (DOE), which is a rigorous statistical technique, is used to analyze effect of several inputs to determine their effects on desired outputs and formulate empirical models. In DOE, one or more measurable output variables of interest are identified. Here input parameters were defined as: tube length (in ft.), tube diameter, (in inches), burst pressure (in psi), and working fluid (specific heat ratio). Output parameters were defined as: peak overpressure (in psi), positive phase duration (in sec.), and positive impulse (in psi*sec). Different levels for each input variables are). Number of experiments that allow all possible combinations of the input factor is determined. All the necessary data is collected. Once the data is collected, Analysis of variance (ANOVA) is performed on the data. ANOVA can be used to identify sources of variation. The analysis of variance table also includes p-values, which are used to determine whether the input factors are significantly related to the output. The p-value was used to drive the decision of whether the input variable had any significant effect on the output. P-value was compared against an alpha value of 0.05. If p-value was lower than 0.05, the input variable was considered significant. If deemed significant, the input variable was included while formulating empirical model. Multiple regression is used to fit the full model based on $Y = a+b_1X_1+b_2X_2+\ldots+b_nX_n$. Here X_n are the input parameters and b_n are the estimated coefficients. A detailed explanation of the method can be found in [39]. Analysis was performed using commercial statistics package, Minitab Inc. (State College, PA, USA)

5.3 Results

5.3.1 Effect of Changing Tube Diameter

Keeping tube length and working fluid constant, the peak overpressure increases as the tube diameter decreases. P-value was compared against an alpha value of 0.05 i.e. within 5%. If the p-value was lower than 0.05, then the factor was significant. Change in tube diameter does not significantly change positive duration or positive impulse. Figure 5:4 shows variation of peak overpressure versus burst pressure for different tube diameter for constant tube length of 20 ft. and air as the working fluid. Figure 5:5 shows variation of peak overpressure versus burst pressure for different tube diameter for constant tube length of 20 ft. and helium as the working fluid. The effect of changing tube diameter is more noticeable at higher burst pressure.

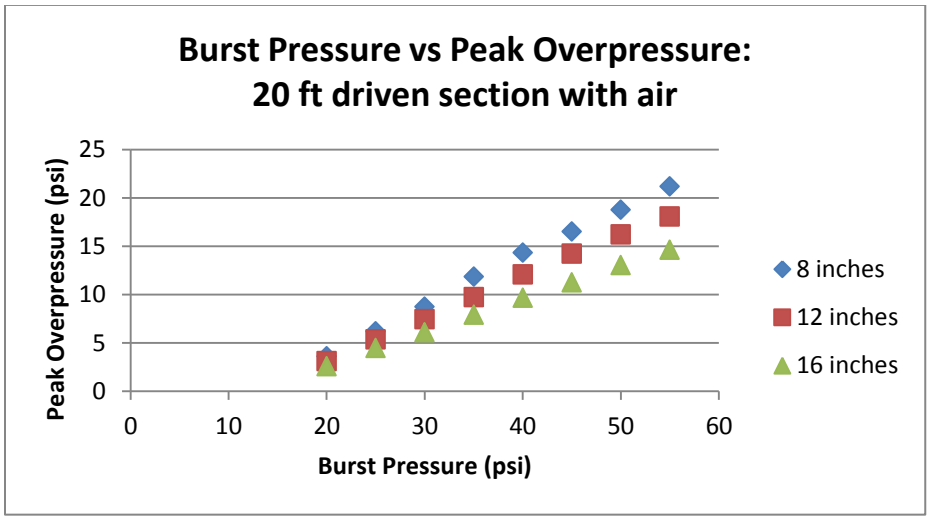

Figure 5:4 Comparison of Computational Peak Overpressure Versus Burst Pressure for Different Tube Diameter for 20 ft. Driver Section with Air

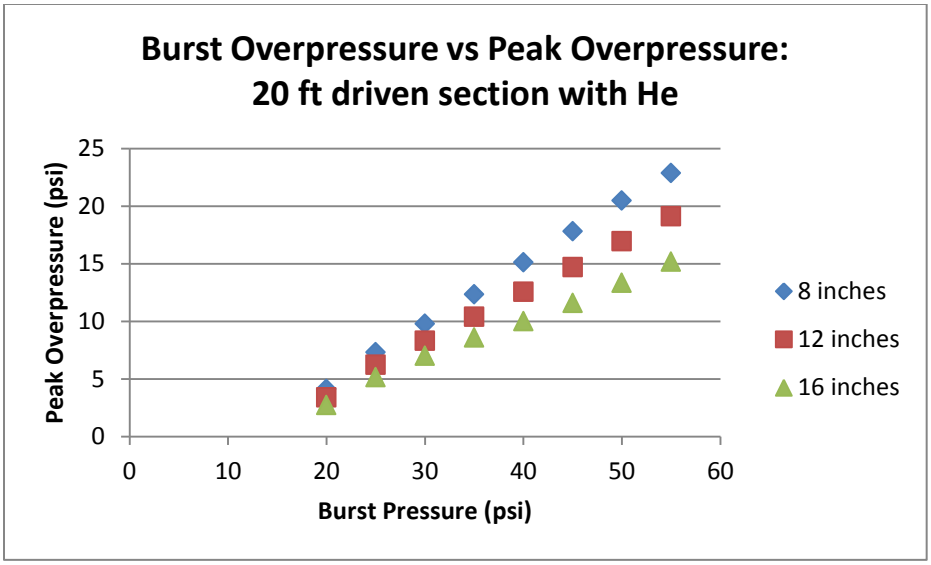

Figure 5:5 Comparison of Computational Peak Overpressure Versus Burst Pressure for Different Tube Diameter for 20 ft. Driver Section with Helium

5.3.2 Effect of Changing Tube Length

Keeping tube diameter and working fluid constant, change in tube length marginally changes the peak overpressure. It does not significantly change positive duration or positive impulse. Figure 5:6 shows variation of peak overpressure versus burst pressure for different tube lengths for constant tube diameter of 12" and air as the working fluid. Figure 5:7 shows variation of peak overpressure versus burst pressure for different tube lengths for constant tube diameter of 12" and helium as the working fluid. These figures are examples of how change in tube length marginally changes the peak overpressure.

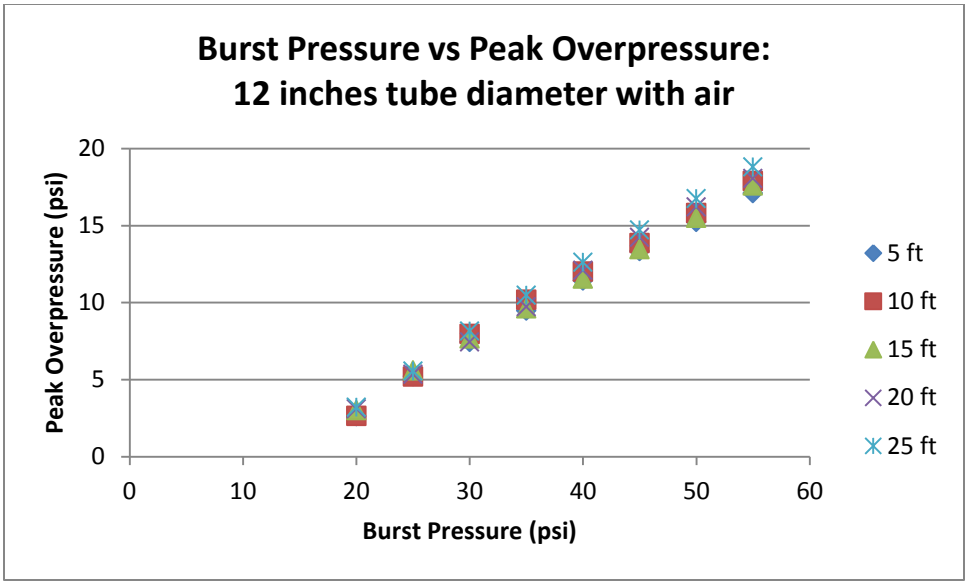

Figure 5:6 Comparison of Computational Peak Overpressure Versus Burst Pressure for Different Tube Length for 12" Driver Section with Air

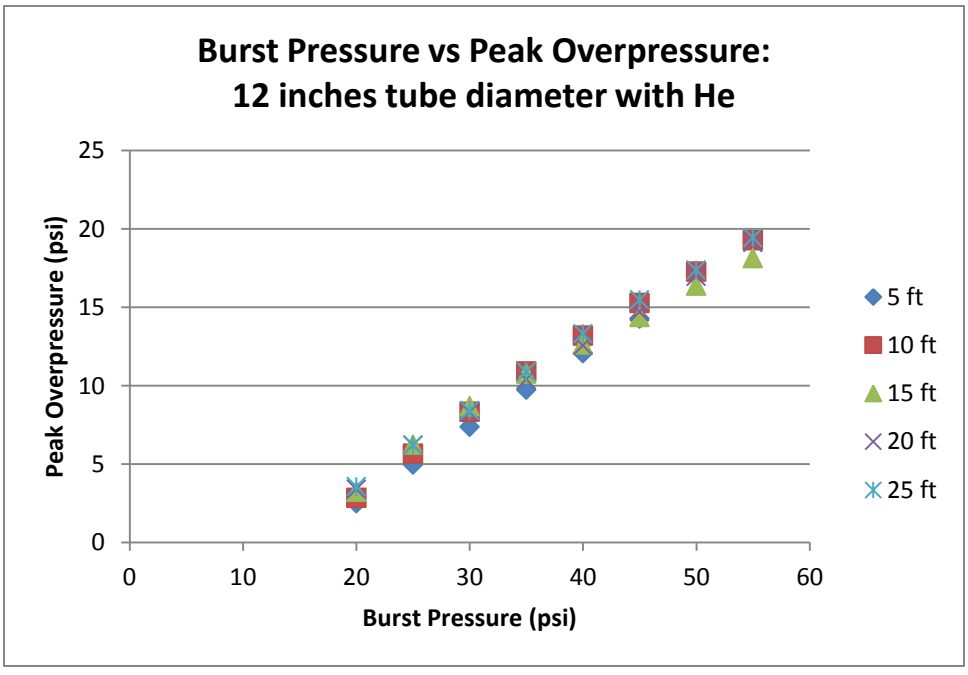

Figure 5:7 Comparison of Computational Peak Overpressure Versus Burst Pressure for Different Tube Length for 12" Driver Section with Helium

5.3.3 Effect of Changing Working Fluid

Looking at the p-value effect of working fluid, and burst pressure was significant on positive phase duration and positive impulse. Table 5:2 presents an example, with tube diameter 8” and 5ft., of how working fluid affects positive impulse. Positive impulse is lower for helium than compressed air. Table 5:3 presents an example, with tube diameter 8” and 5ft., of how working fluid affects positive phase duration. Positive phase duration is lower for helium than compressed air. Tube length and tube diameter were not a very important factor. The negative durations increased as burst pressure increased but not consistently enough to create a very accurate trend.

Table 5:2 The following table provide an example comparing positive phase impulse [psi*sec] for air and helium with tube diameter is 8" and tube length is 5 ft.

Burst pressure (psi)	Air	He
20	0.002021	0.001406
25	0.004458	0.002255
30	0.007192	0.003161
35	0.010177	0.004125
45	0.016916	0.005148
50	0.020644	0.006234
55	0.024572	0.007373

Table 5:3 The following table provide an example comparing positive phase duration [sec] for air and helium with tube diameter is 8" and tube length is 5 ft.

Burst Pressure (psi)	Air	He
20	0.00353	0.00141
25	0.00345	0.00147
30	0.00347	0.00149
35	0.00354	0.00153
45	0.00376	0.00146
50	0.00411	0.00161
55	0.00441	0.00166

5.3.3 Empirical Relations

Table 5:4 summarizes the results of design experiment for output parameter: peak overpressure. Table 5:5 summarizes results of multiple regression for output parameter: positive phase duration.

Table5:6 summarizes results of multiple regression for output parameter: positive impulse. P-value is compared against an alpha value of 0.05 i.e. whithin 5%. If the p-value is lower than 0.05, then the factor is significant. Tube length, tube diameter, working fluid, and burst pressure as well as their interaction is considered to significantly change peak overpressure. Hence, these factors were included while formulating an empirical model for peak overpressure. For positive phase duration and positive impulse, working fluid and burst pressure were considered significant. Hence, the input factors were included for developing empirical models.

Table 5:4 The following table details the p-value for output parameter, peak overpressure, N = 240

Source	P-Value
L	0.04
D	0
gamma	0
Pb	0
L*L	0.011
D*D	0
Pb*Pb	0
L*D	0.037

Table 5:5 The following table details the p-value for output parameter, positive phase duration, N = 240

Source	P-Value
L	0.235
D	0.689
gamma	0
Pb	0.002
L*L	0.815
D*D	0.906
Pb*Pb	0.1270
L*D	0.913

Table 5:6 The following table details the p-value for output parameter, positive impulse, N = 240

Source	P-Value
L	0.557
D	0.064
gamma	0
Pb	0
L*L	0.632
D*D	0.097
Pb*Pb	0.0785
L*D	0.5469

Equation 5.1 is the empirical model for peak overpressure was derived based on design of experiment. The R-squared for equation is 99.59%. Equation 5.2 is the empirical model for positive phase durations was derived based on design of experiment. The R-squared for equation is 94.59%. Equation 5.3 is the empirical model for peak overpressure was derived based on design of experiment. The R-squared for equation is 92.41%. Multiple test cases were simulated. Table 5:7 and Table 5:8 present a test case for validating the empirical relations. Predicted peak overpressure, positive duration, and positive impulse are within 5% of the computational values.

$$\textbf{Peak Overpressure} = -16.26 + 2.059\gamma + L(0.0418 - 0.001381L - 0.001812D + 0.0350\gamma - 0.000059P_b) + D(0.906 - 0.01395D - 0.1966\gamma - 0.019563P_b) + P_b(0.6895 - 0.001587P_b + 0.0629\gamma) \quad \textbf{...}(5.1)$$

$$\textbf{Positive Phase Duration} = 0.017698 - 0.010295\gamma + 0.00002P_b \quad \ldots(5.2)$$

$$\textbf{Positive Impulse} = 0.04125 - 0.03007\gamma + 0.000324P_b \quad \ldots.(5.3)$$

Where,

L is tube length,

D is tube diameter

γ is gamma for working fluid

P_b is burst pressure

Table 5:7 Empirical relation test case: 5ft, 16" tube with air at 60 psi burst pressure

	Predicted	Computational
Peak overpressure	16.304519	15.49807545
Positive duration	0.004485	0.00415
Positive impulse	0.018592	0.015708528

Table 5:8 Empirical relation test case: 15ft, 8” tube with helium at 60 psi burst pressure

	Predicted	Computational
Peak overpressure	24.35093	23.52982
Positive duration	0.001808	0.00181
Positive impulse	0.010774	0.009016

5.4 Discussion

There are numerous shock tube designs that exist for studying bTBI. Some of the tubes utilize explosive sources in shock tube. RDX, Oxyhydrogen [10], and oxy-actelane [40] are some of the common explosive used in shock tubes An advantage of using such shock tubes is that they do not produce a large jet of gas after the shock wave [41]. However, it is very dangerous to use explosives in shock tubes in laboratory setting. In addition, they are very expensive and require specialized training to handle such tubes. Hence, using compressed gas shock tube is a better choice to study bTBI in laboratory setting. However, the pressure time curves produced by compressed gasses differ from those produced by explosives in some cases. The resulting shock wave depends not only on the pressure of the driver at membrane rupture, but also on the dimensions of the shock tube [10]. Effect of varying tube length, tube diameter, burst pressure, working fluid on the blast wave, specifically peak overpressure, positive phase duration, and positive impulse was examined.

Selection of burst pressure was very crucial as it significantly influences peak overpressure, positive impulse, and positive phase duration. As the burst pressure increases, peak overpressure, positive duration, and positive impulse also increases. Burst pressure is directly related to peak overpressure, positive phase duration, and positive impulse.

Design of experiments (DOE) was the method chosen to formulate empirical models related to the shock tube for multiple reasons. DOE is useful in complex phenomena which involve measuring response of manipulating multiple factors at different levels.

Most data-analysis methods only report the process without intervening. However, DOE is a structured way to change process input settings to see the effects it has on the selected output variable. It identifies the important sources of variation and input factors that have little effect on the output parameter. Most important, it can develop an equation to quantify the relationship between the chosen input parameters to the output variable.

The geometrical parameters chosen for shock tube were considered based on design changes that could easily be implemented to the already existing BMEL shock tube. Hence, driver section was neither varied in length nor in diameter. The shock tube is built such that the tube length and tube diameter can be easily varied. To change tube diameter, a coupler between driving and driver section needs to be utilized. An 8" tube diameter, behaves like a converging shock tube. As a shock wave propagates through a tube with decreasing diameter, there is an increase in velocity. Hence, shock strength across this region also increases. Hence, there is an increase in the peak overpressure as compared to 12" tube (see Equation 2.6). An 16" tube diameter, behaves like a diverging shock tube. The computational domain considered the real-life design implementation. For peak overpressure, positive duration, and positive impulse did not change significantly with variation in tube length. When the effect of tube diameter was evaluated, increase in diameter significantly decreased the peak overpressure. Hence, it was found that peak overpressure is inversely related to tube diameter. Variation in tube diameter did not have any significant impact on positive impulse and duration. Velocity

is directly proportional to gamma (see Equation 2.1). Gamma for helium is 1.66 and air is 1.4. Hence, velocity is higher for helium.

The two main gases used in shock tube are compressed air and helium. Hence, these gases were selected as working fluid to create the empirical model. Compressed air is very cheap and readily available. It has used in medical shocks to evaluate the effects of blasts since 1949 [42, 43]. However, one of the drawbacks of using compressed air is that it is not an ideal gas. The flattening of the peak is noticed before the decay; hence, the positive phase duration of the overpressure is greater for compressed air. Even though compressed air is convenient, it is important to note that the shock wave characteristics of compressed air deviate from those caused by the explosives being modeled. One of the ways to solve this problem is to use helium. But, even nearly ideal gasses like helium can cause undesirable effects. For example, use of helium as the driving gas results in a hypoxic environment around the test subject for some time after the shock. This could potentially cause additional confounding injury [10]. Peak overpressure is slightly higher for Helium than for compressed air. Positive duration as well as impulse are higher for compressed air than Helium.

Model is valid only for a shock tube that resembles Robbins-Moreno shock tube configuration, which uses a single Mylar membrane with mechanical rupture. It has been computationally tested for burst pressure between 20 and 60 psi, tube length between 5 and 25 ft., and tube diameter between 8 and 16 inches Only Helium and Air has been tested as working fluid. For all the features, working fluid has a significant influence. But, these computational model did not consider mixing in case of helium. Including the

mixing of the gases will have an impact on the model. In future, mixing will be included. The empirical models developed in this thesis will also be experimentally validated. Also, due to randomness in the data, empirical model for negative phase was not developed.

The empirical models formulated using CFD models of the shock tube provide reasonable predictions about the key features of a pressure profile that and their dependence on the shock tube geometry, working fluid, and burst pressure. This knowledge will be used to construct a shock tube to better replicate the pressure profiles of ordnance for animal studies of bTBI.

CHAPTER VI

SUMMARY

The pathology of bTBI is poorly understood. One way to study it is to construct shock tubes that replicate explosive's blast pressure profile. Our group, at Biomechanical Environments Laboratory, has designed and constructed an MRI compatible shock tube to investigate the cumulative effects of explosive blast exposure on the brain and spinal cord.

6.1 One Dimensional Shock Tube: Summary

The goal of this study was to review current state of numerical schemes for modelling compressible Euler equation in terms of their fundamental properties for one-dimensional shock tube. It compares them in terms of accuracy, efficiency, and ease in implementation. AUSM and Roe scheme were found to be most accurate and efficient for modelling shock waves.

6.2 Two Dimensional Shock Tube: Summary

The goal of this study was to develop 2D computational models to simulate the shock wave propagation in our shock tube. Preliminary simulations were developed and executed for our circular cylindrical shock tube in the 20ft configuration. Computations were carried out using Star CCM+. The propagation of shock wave in the shock tube

was modeled as unsteady, compressible, axisymmetric flow with time-step of $1e^{-5}$ seconds. Data was post-processed in MATLAB. Fully-ruptured membrane model was compared with half-ruptured membrane model. The peak overpressure for both these models was compared with experimental model. It was concluded the half-ruptured membrane model better replicates the experimental results.

6.3 Optimization of Shock Tube: Summary

The goal of this research is to develop the shock tube as a better model for replicating the pressure profiles of military ordinance using Computational Fluid Dynamics (CFD) models. Various 2D models to simulate the shock wave propagation in a shock tube and determine the effects of tube length and diameter as well as working fluid on pressure profiles were developed. Ranges of different parameters evaluated are: Tube length; 5, 10, 15, 20, and 25 feet; Tube diameter; 8", 12", 16"; working fluid; compressed air and helium; burst pressure; 20, 25, 30, 35, 40, 45, 50, 55 psi. A total of 240 simulations were run to evaluate the effect of these factors on the pressure profile. Computations were carried out using commercial software, Star CCM+ (CD-adapco, NY, USA). The propagation of shock wave in the shock tube was modeled as unsteady, inviscid, compressible, axisymmetric flow with time-step of $1e^{-5}$ seconds. Data was post-processed in MATLAB. Multiple regression was run on these parameters to establish empirical relationship with pressure profile. The effects of changing burst pressure, tube length, tube diameter, and working fluid were evaluated on key features of the pressure profile (peak overpressure, positive phase duration, and impulse). As the burst pressure

increases, peak overpressure, positive phase duration, and impulse also increase. Increasing the tube diameter decreases the peak overpressure as well. Change in tube length does not have a significant effect on peak overpressure, positive phase duration, and impulse. Working fluid was the most significant factor determining the magnitude of impulse and duration. The empirical formulas for peak overpressure, positive phase duration, and positive impulse were developed. These formulas using CFD model of the shock tube provide reasonable predictions about the key features of a pressure profile that and their dependence on the shock tube geometry, working fluid, and burst pressure. This knowledge will be used to construct a shock tube to better replicate the pressure profiles of ordnance for animal studies of bTBI.

REFERENCES

[1] *Returning home from Iraq and Afghanistan: Preliminary assessment of readjustment needs of veterans, service members, and their families*. Washington, D.C.: National Academies Press, 2010.

[2] E. Bagalman, "Traumatic brain injury among veterans.," Congressional Research Service 2013.

[3] R. G. DePalma, D. G. Burris, H. R. Champion, and M. J. Hodgson, "Current concepts: Blast injuries," *New England Journal of Medicine*, vol. 352, pp. 1335-1342, Mar 2005.

[4] I. Cernak and L. J. Noble-Haeusslein, "Traumatic brain injury: An overview of pathobiology with emphasis on military populations," *J Cereb Blood Flow Metab*, vol. 30, pp. 255-66, Feb 2010.

[5] J. Guidera, "A veteran's new take on bTBI," in *Harvard Science Review*, ed, 2011, pp. 38-40.

[6] M. Chavko, W. A. Koller, W. K. Prusaczyk, and R. M. McCarron, "Measurement of blast wave by a miniature fiber optic pressure transducer in the rat brain," *Journal of Neuroscience Methods*, vol. 159, pp. 277-281, Jan 2007.

[7] R. A. Bauman, G. Ling, L. Tong, A. Januszkiewicz, D. Agoston, N. Delanerolle, *et al.*, "An introductory characterization of a combat-casualty-care relevant swine model of closed head injury resulting from exposure to explosive blast," *Journal of Neurotrauma*, vol. 26, pp. 841-860, Jun 2009.

[8] A. D. C. Leonardi, C. Bir, D. Ritzel, and P. VandeVord, "Intracranial pressure increases during exposure to a shock wave," *Journal of Neurotrauma,* vol. 28, pp. 85-94, 2011.

[9] J. Long, T. Bentley, K. Wessner, C. Cerone, S. Sweeney, and R. Bauman, "Blast overpressure in rats: Recreating a battlefield injury in the laboratory," *Journal of Neurotrauma,* vol. 26, pp. 827-40, 2009.

[10] D. V. Reneer, R. D. Hisel, J. M. Hoffman, R. J. Kryscio, B. T. Lusk, and J. W. Geddes, "A multi-mode shock tube for investigation of blast-induced traumatic brain injury," *Journal of Neurotrauma,* vol. 28, pp. 95-104, Jan 2011.

[11] W. E. Baker, *Explosions in air*. Austin. University of Texas Press, 1973.

[12] J. E. A. John, *Gas dynamics*. Upper Saddle River, N.J. : Pearson Prentice Hall, 2006.

[13] M. Risling, S. Plantman, M. Angeria, E. Rostami, B. M. Bellander, M. Kirkegaard, *et al.*, "Mechanisms of blast induced brain injuries, experimental studies in rats," *Neuroimage,* vol. 54 Suppl 1, pp. S89-97, Jan 2011.

[14] Y. Wang, Y. Wei, S. Oguntayo, W. Wilkins, P. Arun, M. Valiyaveettil, *et al.*, "Tightly coupled repetitive blast-induced traumatic brain injury: Development and characterization in mice," *Journal of Neurotrauma,* vol. 28, pp. 2171-83, Oct 2011.

[15] M. S. Chafi, G. Karami, and M. Ziejewski, "Biomechanical assessment of brain dynamic responses due to blast pressure waves," *Annals of Biomedical Engineering,* vol. 38, pp. 490-504, Feb 2010.

[16] A. C. Courtney and M. W. Courtney, "A thoracic mechanism of mild traumatic brain injury due to blast pressure waves," *Med Hypotheses,* vol. 72, pp. 76-83, Jan 2009.

[17] K. H. T. D. L. W. R. A. Hurley, "Blast-related Traumatic Brain Injury: What is known," *J Neuropsychiatry Clin Neurosci* vol. 18, 2006.

[18] R. A. Stern, D. O. Riley, D. H. Daneshvar, C. J. Nowinski, R. C. Cantu, and A. C. McKee, "Long-term consequences of repetitive brain trauma: Chronic traumatic encephalopathy," *PM R,* vol. 3, pp. S460-7, Oct 2011.

[19] J. Mediavilla Varas, M. Philippens, S. R. Meijer, A. C. van den Berg, P. C. Sibma, J. L. van Bree, *et al.*, "Physics of IED blast shock tube simulations for mTBI research," *Front Neurol,* vol. 2, p. 58, 2011.

[20] P. D. Lax, "Weak solutions of non-linear hyperbolic equations and their numerical computation," *Communications on Pure and Applied Mathematics,* vol. 7, pp. 159-193, 1954.

[21] P. Lax and B. Wendroff, "Systems of conservation laws," *Communications on Pure and Applied Mathematics,* vol. 13, pp. 217-237, 1960.

[22] R. Richtmyer, "A survey of difference methods for nonsteady fluid dynamics," in *NCAR Technical Notes*, N. C. f. A. Research, Ed., ed. Coulder, Colorado, 1962.

[23] M.-S. Liou and C. Steffen, "A New Flux Splitting Scheme," *Journal of Computational Physics,* vol. 107, pp. 23-39, 1993.

[24] E. F. Toro, "The Riemann problem for the Euler equations," in *Riemann Solvers and Numerical Methods for Fluid Dynamics a Practical Introduction*, Berlin: Springer, 2006, pp. 115-162.

[25] P. J. Petrie-Repar and P. A. Jacobs, "A computational study of shock speeds in high-performance shock tubes," *Shock Waves*, vol. 8, pp. 79-91, Apr 1998.

[26] R. S. M. Chue and G. Eitelberg, "Studies of the transient flows in high enthalpy shock tunnels," *Experiments in Fluids*, vol. 25, pp. 474-486, Oct 1998.

[27] J. Tretjakovas, B. Baksys, A. Bargelis, R. Jonusas, S. Bockus, M. Leonavicius, A. Ziliukas, *et al.*, "Determining the falling pressure in the gas shock tube during the rupture of its diaphragm," in *Mechanika 2012: Proceedings of the 17th International Conference*, Kaunas Univ Technology Press, 2012, pp. 312-315.

[28] E. M. Rothkopf and W. Low, "Diaphragm opening process in the shock-tube," *Physics of Fluids*, vol. 17, pp. 1169-1173, 1974.

[29] R. Brun and R. Reboh, "Influence of diaphragm opening process on intial flow of shock tubes," *Mechanics Research Communications*, vol. 3, pp. 215-219, 1976.

[30] A. Rajagopal, "Computational study on micro shock tube flows with gradual diaphragm rupture process," *Open Journal of Fluid Dynamics*, vol. 02, pp. 235-241, 2012.

[31] R. H. Garman, L. W. Jenkins, R. C. Switzer, 3rd, R. A. Bauman, L. C. Tong, P. V. Swauger, *et al.*, "Blast exposure in rats with body shielding is characterized primarily by diffuse axonal injury," *Journal of Neurotrauma*, vol. 28, pp. 947-59, Jun 2011.

[32] K. J. Gerhardt, R. M. Abrams, X. Y. Huang, S. K. Griffiths, and A. J. M. Peters, "Intra-abdominal sound pressure levels during impulse noise exposure in sheep," *Military Medicine,* vol. 165, pp. 153-156, Feb 2000.

[33] S. M. Moochhala, S. Md, J. Lu, C. H. Teng, and C. Greengrass, "Neuroprotective role of aminoguanidine in behavioral changes after blast injury," *Journal of Trauma-Injury Infection and Critical Care,* vol. 56, pp. 393-403, Feb 2004.

[34] I. Cernak, Z. G. Wang, J. X. Jiang, X. W. Bian, and J. Savic, "Ultrastructural and functional characteristics of blast injury-induced neurotrauma," *Journal of Trauma-Injury Infection and Critical Care,* vol. 50, pp. 695-706, Apr 2001.

[35] J. M. Cheng, J. W. Gu, Y. A. Ma, T. Yang, Y. Q. Kuang, B. C. Li, *et al.*, "Development of a rat model for studying blast-induced traumatic brain injury," *Journal of the Neurological Sciences,* vol. 294, pp. 23-28, Jul 2010.

[36] A. Saljo, M. Mayorga, H. Bolouri, B. Svensson, and A. Hamberger, "Mechanisms and pathophysiology of the low-level blast brain injury in animal models," *Neuroimage,* vol. 54 Suppl 1, pp. S83-8, Jan 2011.

[37] J. K. Zhang, Z. G. Wang, H. G. Leng, and Z. H. Yang, "Studies on lung injuries caused by blast underpressure," *Journal of Trauma-Injury Infection and Critical Care,* vol. 40, pp. S77-S80, Mar 1996.

[38] E. Gruss, "A correction for primary blast injury criteria," *Journal of Trauma-Injury Infection and Critical Care,* vol. 60, pp. 1284-1289, Jun 2006.

[39] R. E. Bechhofer, T. J. Santner, and D. M. Goldsman, *Design and Analysis of Experiments for Statistical Selection, Screening, and Multiple Comparisons*: Wiley New York, 1995.

[40] A. C. Courtney, L. P. Andrusiv, and M. W. Courtney, "Oxy-acetylene driven laboratory scale shock tubes for studying blast wave effects," *Rev Sci Instrum,* vol. 83, p. 045111, Apr 2012.

[41] M. W. Courtney and A. C. Courtney, "Working toward exposure thresholds for blast-induced traumatic brain injury: Thoracic and acceleration mechanisms," *Neuroimage,* vol. 54, pp. S55-S61, Jan 2011.

[42] B. Cassen, L. Curtis, and K. Kistler, "Initial studies of the effect of laboratory produced air blast on animals," 1949.

[43] H. Celander, C. J. Clemedson, U. A. Ericsson, and H. I. Hultman, "The use of a compressed air operated shock tube for physiological blast research," *Acta physiologica Scandinavica,* vol. 33, pp. 6-13, 1955.

APPENDIX A

A.1 Van Leer

Figure A:A:1 shows numerical solution using Van Leer scheme for grid resolution n = 601, and CFL number = 0.1 in comparison to Riemann solution. FigureA:2 shows solution Van Leer scheme for grid resolution n = 601, and CFL number = 0.95 in comparison to Riemann solution. Refining the grid size better captures the sharp gradients. Hence, higher grid resolution was used to evaluate the effect of CFL. Changing CFL number does not produce any appreciable effect on the solution. It provides an improvement over solution from finite difference methods.

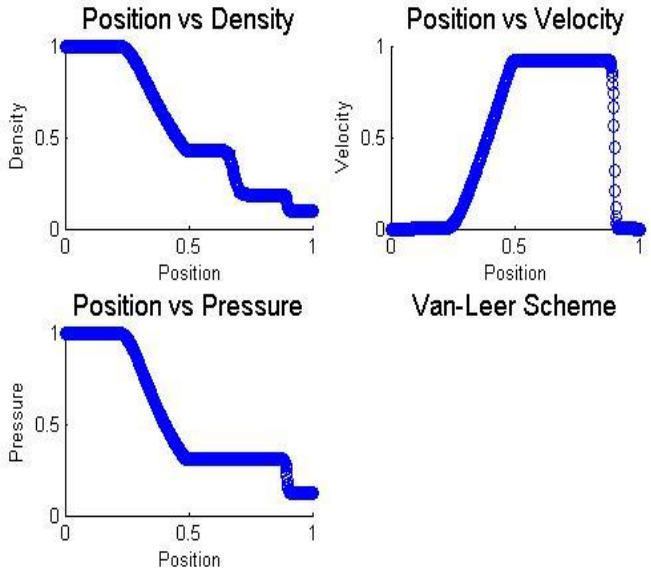

Figure A:1 The Solutions by Van Leer Scheme with CFL = 0.1

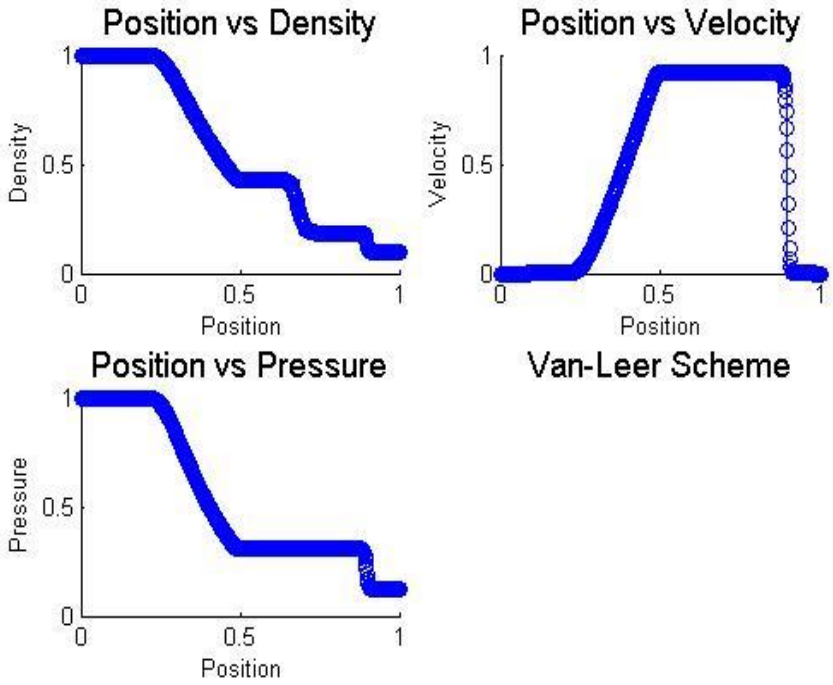

Figure A:2 The Solutions by Van Leer Scheme with CFL = 0.95

A.2 Roe

FigureA:3 shows numerical solution using Roe scheme for grid resolution n = 601, and CFL number = 0.1 in comparison to Riemann solution. FigureA:4 shows solution Roe scheme for grid resolution n = 601, and CFL number = 0.95 in comparison to Riemann solution. Refining the grid size better captures the sharp gradients. Hence, higher grid resolution was used to evaluate the effect of CFL. Changing CFL number does not produce any appreciable effect on the solution. It provides an improvement over solution from finite difference methods. It is easier to implement in comparison to Van Leer scheme.

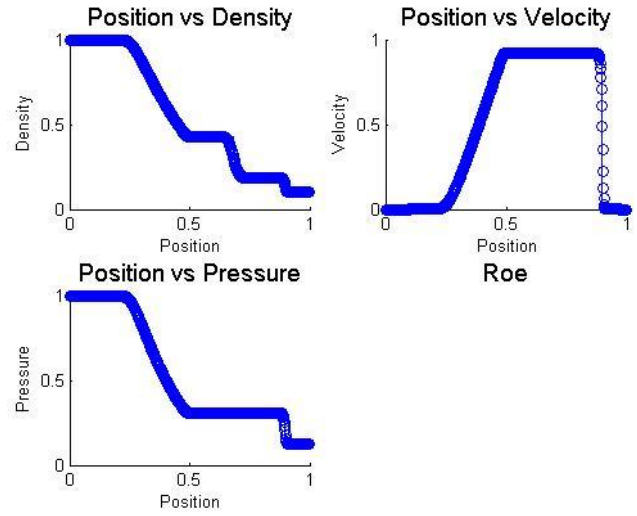

Figure A:3 The Solutions by Roe Scheme with CFL = 0.1

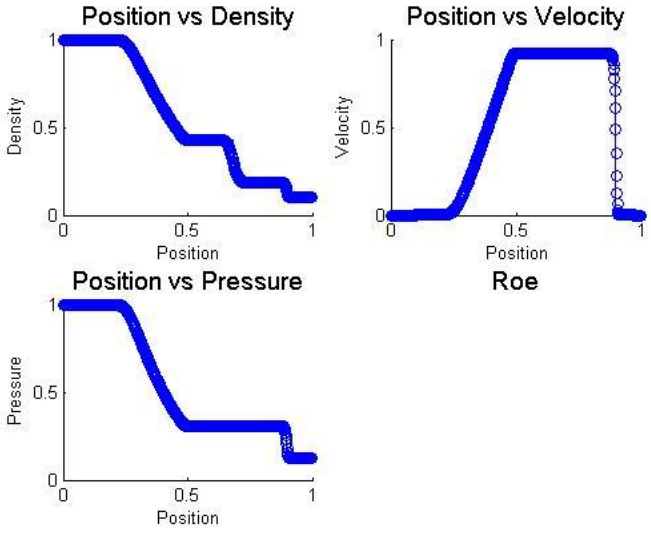

Figure A:4 The Solutions by Roe Scheme with CFL = 0.95

A.3 Osher

FigureA:5 shows numerical solution using Osher scheme for grid resolution n = 601, and CFL number = 0.1 in comparison to Riemann solution. FigureA:6 shows solution Osher scheme for grid resolution n = 601, and CFL number = 0.95 in comparison to Riemann solution. Refining the grid size better captures the sharp gradients. Hence, higher grid resolution was used to evaluate the effect of CFL. It provides an improvement over solution from finite difference methods.

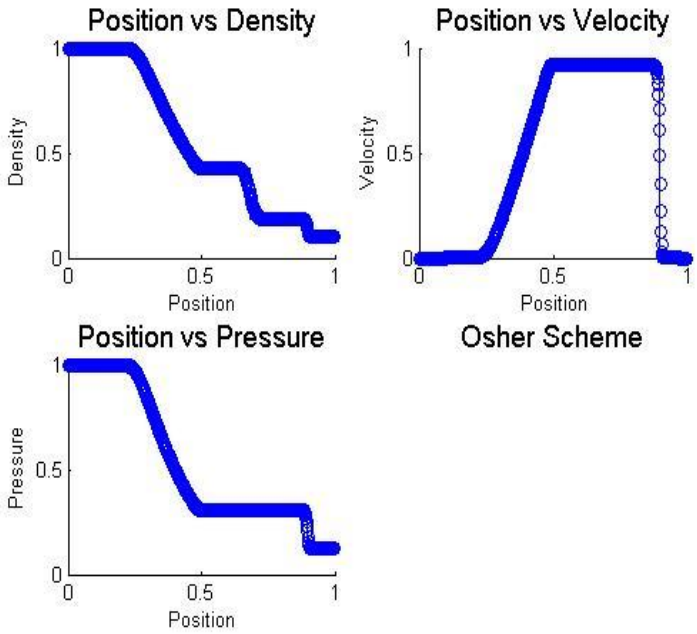

Figure A:5 The Solutions by Osher Scheme with CFL = 0.1

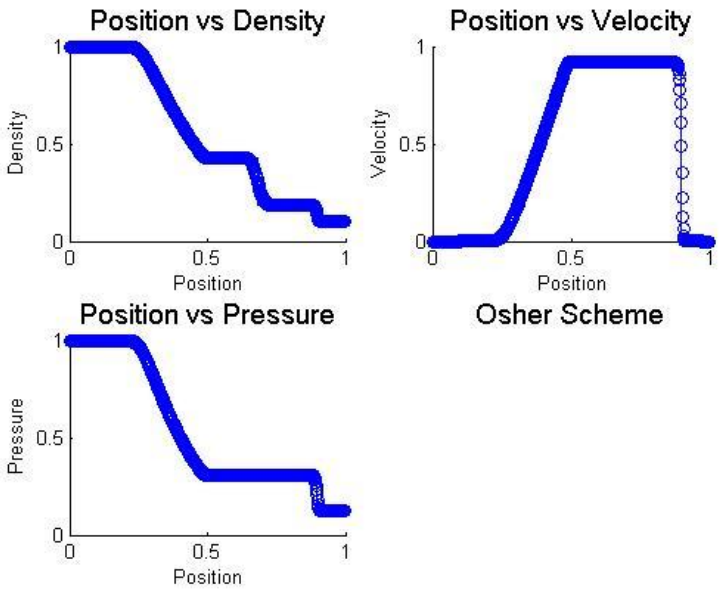

Figure A:6 The Solutions by Osher Scheme with CFL = 0.95

A.4 AUSM

FigureA:7 shows numerical solution using AUSM scheme for grid resolution n = 601, and CFL number = 0.1 in comparison to Riemann solution. FigureA:8 shows solution AUSM scheme for grid resolution n = 601, and CFL number = 0.95 in comparison to Riemann solution. Refining the grid size better captures the sharp gradients. Hence, higher grid resolution was used to evaluate the effect of CFL. It provides an improvement over solution from finite difference methods.

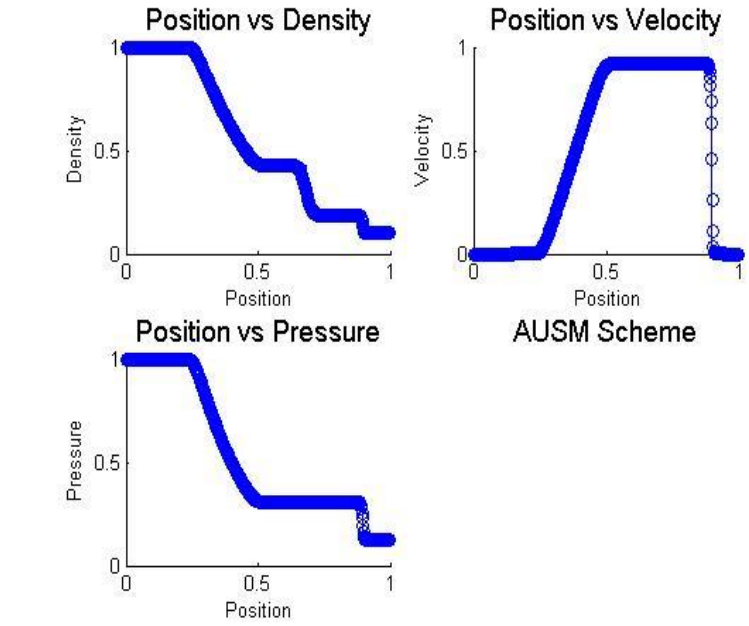

Figure A:7 The Solutions by AUSM Scheme with CFL = 0.1

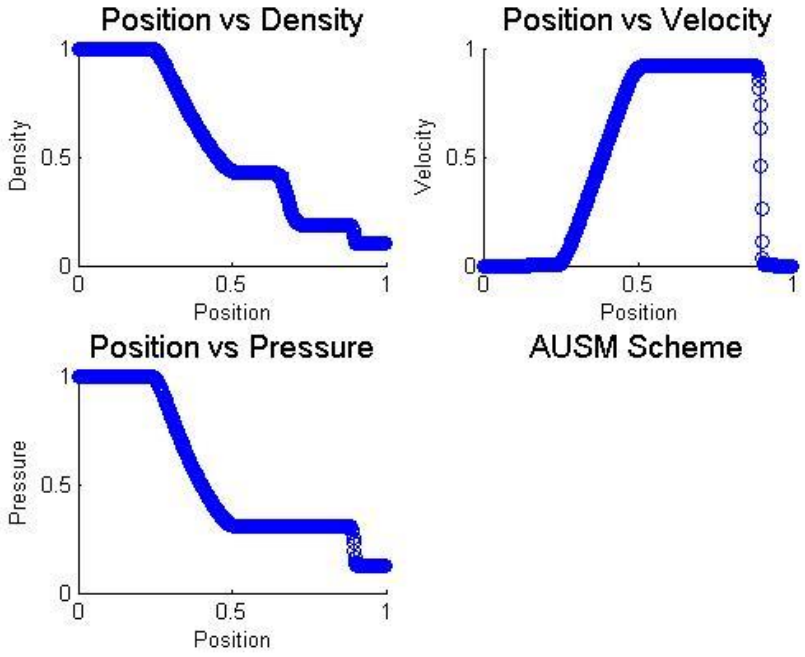

Figure A:8 The Solutions by AUSM Scheme with CFL = 0.95

APPENDIX B

B.1 Pressure profiles along the radius of the outlet

We obtained data from multiple points along the radius of the shock tube to establish that pressure profile is insensitive to this location. The distance corresponds to where the animal will be placed in during the experiments. As seen in Figure B:1, We compared the blast wave profile along the radius of the tube at the outlet. It was observed that there was no difference in wave profiles near the outlet. This height of the probe will not affect the wave profile.

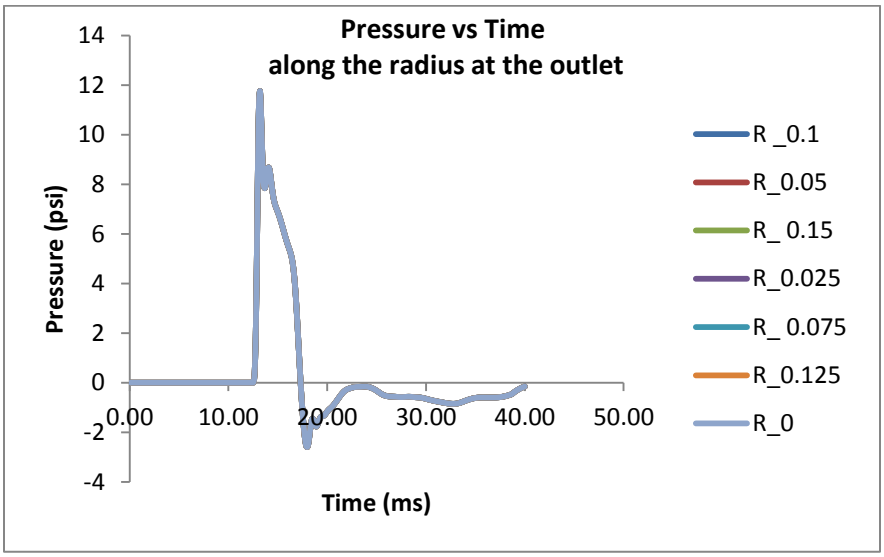

Figure B:1 Overpressure vs Time Along the Radius of the Shock Tube at the Outlet

B.2 Inviscid vs. Viscid

We compared the blast wave profile in a tube with flow modeled as both inviscid and viscous model. As seen in Figure B:2, it was observed that there was no major variation between the two models. This suggests that viscosity of the fluid does not play a significant role in blast-wave propagation.

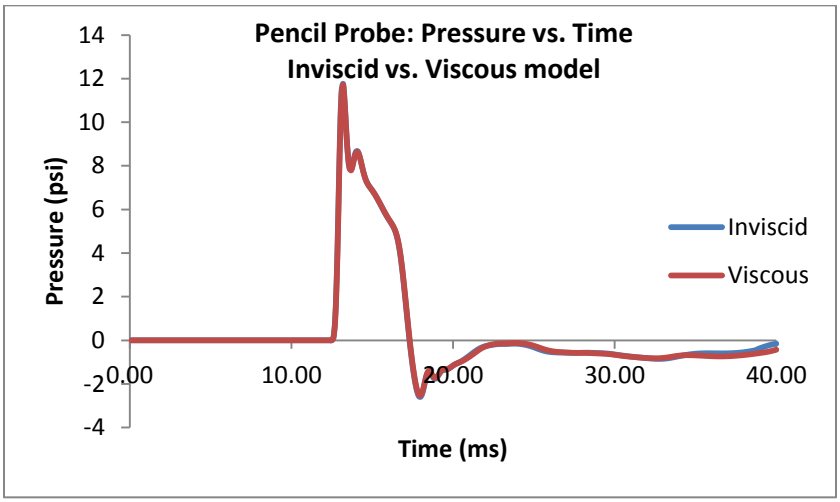

Figure B:2 Overpressure vs. Time for Inviscid Against Viscous Model

B.3 Experimental vs Computational

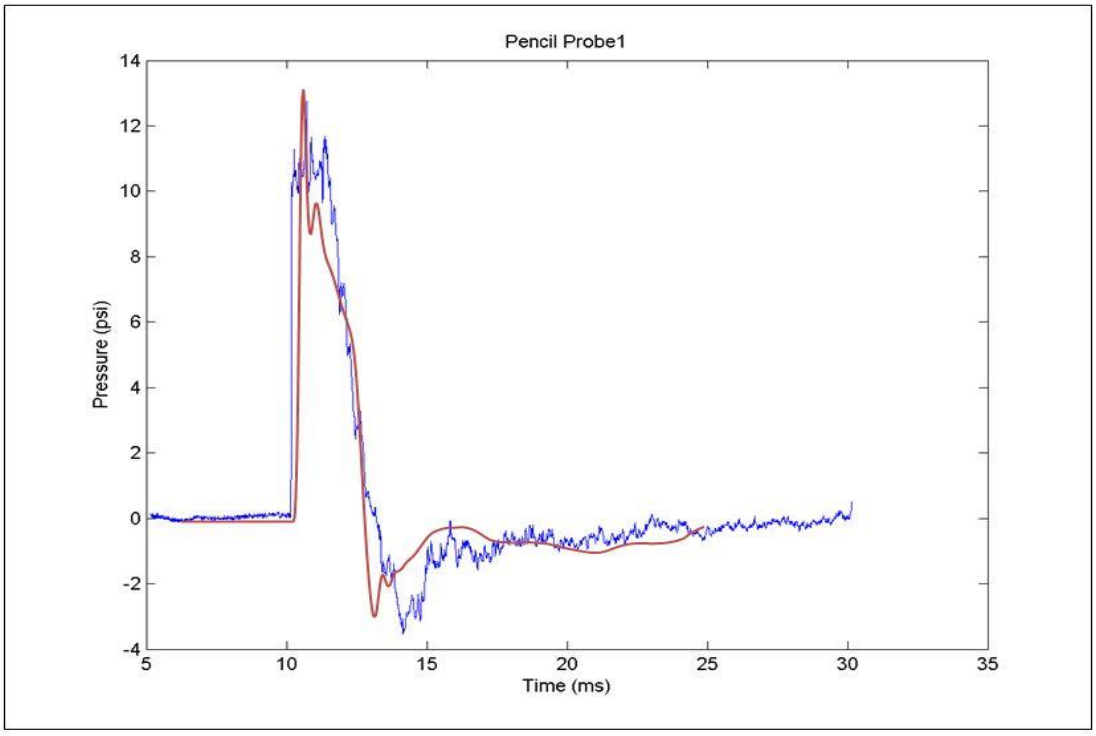

Figure B:3 Comparison of Experimental (blue) with Computaional (red) Pressure Profile for Sensor 4 for Burst Pressure of 37.5psi and Air as Working Fluid

APPENDIX C

Table C:1 presents the location of sensor from where data was obtained.

Table C:1 Location of points from where was obtained data

Driven Section 5 ft.	
	distance from inlet (ft.)
Sensor 1	2.26
Sensor 2	3.28
Sensor 3	4.92
Sensor 4	6.23
Driven Section 10 ft.	
	distance from inlet (ft.)
Sensor 1	2.26
Sensor 2	5.68
Sensor 3	9.19
Sensor 4	10.23
Driven Section 15 ft.	
	distance from inlet (ft.)
Sensor 1	2.26
Sensor 2	5.68
Sensor 3	14.06
Sensor 4	15.99
Driven Section 20 ft.	
	distance from inlet (ft.)
Sensor 1	2.26
Sensor 2	5.68
Sensor 3	14.06
Sensor 4	20.93
Driven Section 25 ft.	
	distance from inlet (ft.)
Sensor 1	2.26
Sensor 2	5.68
Sensor 3	14.06
Sensor 4	25.93

C.1 Effect of changing tube diameter

Table C:2 shows variation of peak overpressure versus burst pressure for different tube diameter for constant tube length of 5 ft. Table C:3 shows variation of peak overpressure versus burst pressure for different tube diameter for constant tube length of 10 ft. Table C:4 shows variation of peak overpressure versus burst pressure for different tube diameter for constant tube length of 15 ft. Table C:5 shows variation of peak overpressure versus burst pressure for different tube diameter for constant tube length of 20 ft. . Table C:6 shows variation of peak overpressure versus burst pressure for different tube diameter for constant tube length of 25 ft. and helium as the working fluid. Peak overpressure decreases with increasing tube diameter.

C.2 Effect of changing tube length

Figure C: 1 – C:8 shows effect of changing tube diameter on peak overpressure. Figure 9 shows variation of peak overpressure versus burst pressure for different tube lengths for constant tube diameter of 8” and air as the working fluid. Figure 10 shows variation of peak overpressure versus burst pressure for different tube lengths for constant tube diameter of 8” and helium as the working fluid. Figure 11 shows variation of peak overpressure versus burst pressure for different tube lengths for constant tube diameter of 16” and air as the working fluid. Figure 12 shows variation of peak overpressure versus burst pressure for different tube lengths for constant tube diameter of 16” and helium as the working fluid.

Table C:2 Comparison of computational peak overpressure versus burst pressure for different tube diameter (5 ft. driver section)

Burst Pressure (psi)	Peak Overpressure (psi)	
	Air	He
8 inches		
20	2.8792	3.5635
25	5.4271	5.8905
30	8.1152	8.8151
35	10.8935	11.5957
40	13.5314	14.2665
45	16.0382	16.8068
50	18.6141	19.2595
55	21.0540	21.6274
12 inches		
20	2.6199	2.6990
25	5.2112	5.9642
30	7.4325	7.3767
35	9.4863	9.7488
40	11.4419	12.0738
45	13.3541	14.2785
50	15.2308	16.7504
55	17.1047	19.1104
16 inches		
20	2.1593	1.9999
25	4.1527	3.9335
30	6.0275	5.8490
35	7.8241	7.6950
40	9.5167	9.5495
45	11.0954	11.3304
50	12.5638	13.0434
55	13.9507	14.6581

Table C:3 Comparison of computational peak overpressure versus burst pressure for different tube diameter (10 ft. driver section)

Burst Pressure (psi)	Peak Overpressure (psi)	
	Air	He
8 inches		
20	3.0790	3.4882
25	6.4398	6.9446
30	9.2716	10.0431
35	11.7113	12.7133
40	14.0770	15.2113
45	16.2850	17.3593
50	18.4365	19.0158
55	20.6269	21.7377
12 inches		
20	2.6375	2.8426
25	5.1914	5.6690
30	7.9650	8.3423
35	10.1923	10.9042
40	12.0165	13.1915
45	13.8662	15.2779
50	15.8253	17.2809
55	17.9013	19.2893
16 inches		
20	2.1029	2.3475
25	4.3295	4.6560
30	6.4488	6.8705
35	8.1399	8.9271
40	9.8190	10.7222
45	11.5267	12.4099
50	13.2665	13.9847
55	14.7941	15.4869

Table C:4 Comparison of computational peak overpressure versus burst pressure for different tube diameter (15 ft. driver section)

Burst Pressure (psi)	Peak Overpressure (psi)	
	Air	He
8 inches		
20	3.5569	3.8189
25	6.4722	7.2363
30	8.7534	9.9190
35	10.8153	12.1280
40	12.9536	14.2617
45	15.3964	16.5386
50	18.1712	18.8226
55	20.7979	21.0557
12 inches		
20	3.0180	3.2362
25	5.5831	6.2310
30	7.6794	8.6949
35	9.6269	10.7730
40	11.5630	12.6199
45	13.4730	14.3857
50	15.5039	16.3768
55	17.6149	18.1481
16 inches		
20	2.3644	2.3470
25	4.7153	4.6546
30	6.2676	6.8681
35	7.8482	8.9080
40	9.4780	10.4604
45	11.0065	11.8596
50	12.4447	13.3274
55	14.0103	14.6307

Table C:5 Comparison of computational peak overpressure versus burst pressure for different tube diameter (20 ft. driver section)

Burst Pressure (psi)	Peak Overpressure (psi)	
	Air	He
8 inches		
20	3.6148	4.1119
25	6.1745	7.3014
30	8.7251	9.8023
35	11.8496	12.3417
40	14.3436	15.1161
45	16.5272	17.8331
50	18.7791	20.4790
55	21.1985	22.8880
12 inches		
20	3.1075	3.3990
25	5.3488	6.2220
30	7.4520	8.3155
35	9.7345	10.3944
40	12.0982	12.5640
45	14.2391	14.7081
50	16.2143	16.9723
55	18.0721	19.1438
16 inches		
20	3.1075	3.3990
25	5.3488	6.2220
30	7.4520	8.3155
35	9.7345	10.3944
40	12.0982	12.5640
45	14.2391	14.7081
50	16.2143	16.9723
55	18.0721	19.1438

Table C:6 Comparison of computational peak overpressure versus burst pressure for different tube diameter (25 ft. driver section)

Burst Pressure (psi)	Peak Overpressure (psi)	
	Air	He
8 inches		
20	3.5838	4.0595
25	6.1235	6.9385
30	9.1551	9.5489
35	11.3985	12.3629
40	13.7071	15.0003
45	16.3086	17.4012
50	18.7593	19.5951
55	20.8888	22.5550
12 inches		
20	3.2031	3.5602
25	5.5503	6.2048
30	8.1534	8.4268
35	10.4742	10.8995
40	12.6127	13.3242
45	14.7098	15.4861
50	16.7485	17.3844
55	18.8020	19.4457
16 inches		
20	2.5656	2.8156
25	4.3105	5.0650
30	6.2261	6.7638
35	8.0575	8.3972
40	9.6811	10.2012
45	11.3830	11.9841
50	12.8878	13.5970
55	14.2515	15.1593

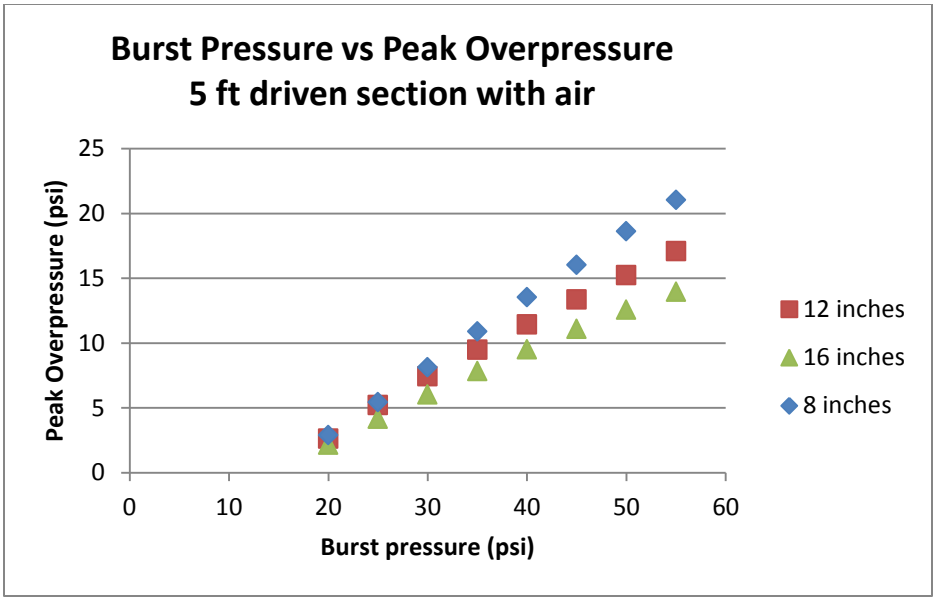

Figure C:1 Comparison of Computational Peak Overpressure Versus Burst Pressure for Different Tube Diameter (5 ft. Driver Section - Air)

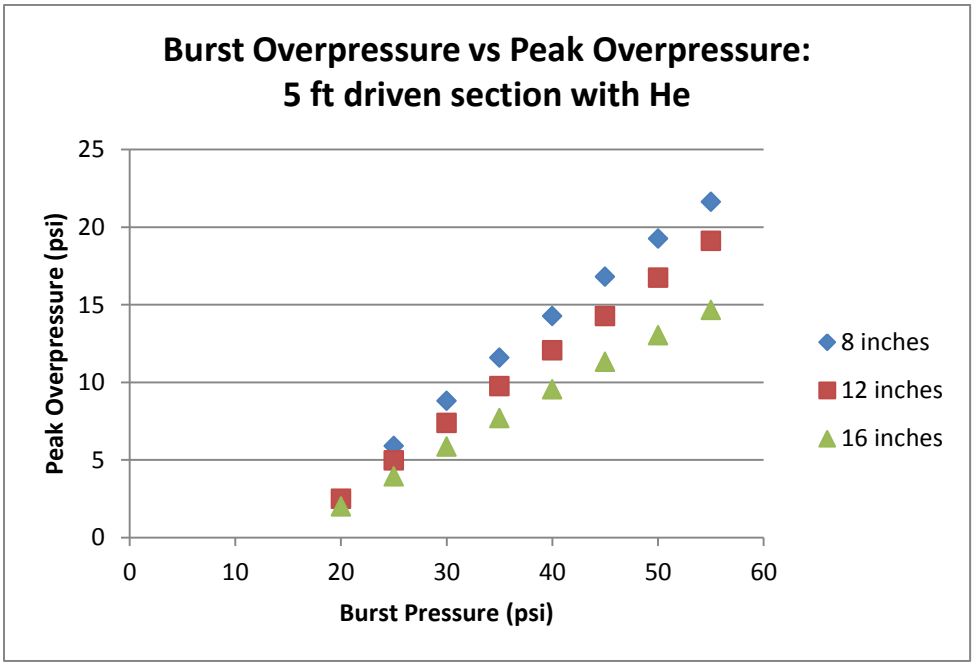

Figure C:2 Comparison of Computational Peak Overpressure Versus Burst Pressure for Different Tube Diameter (5 ft. Driver Section – Helium)

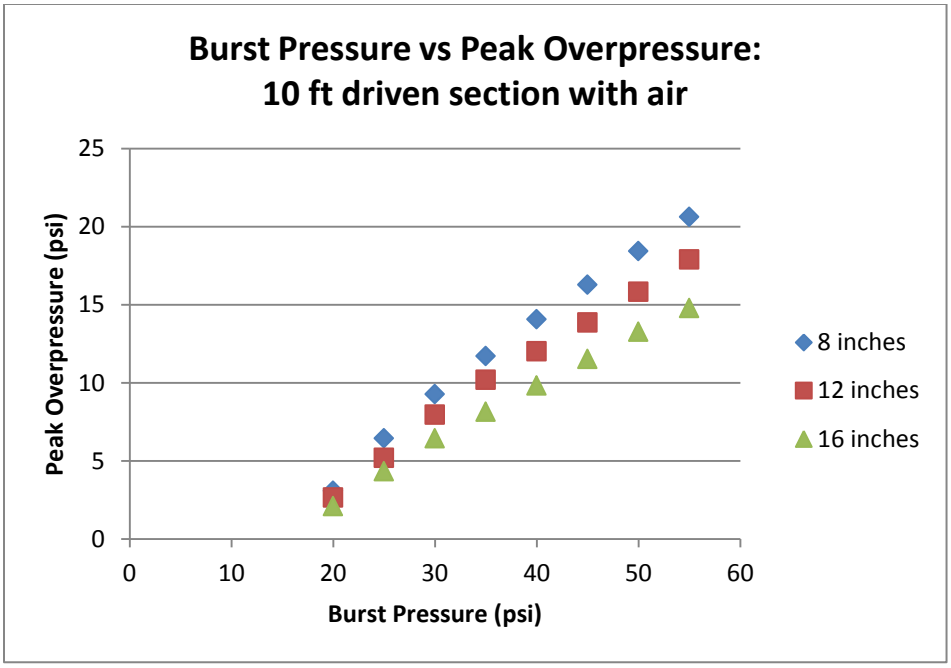

Figure C:3 Comparison of Computational Peak Overpressure Versus Burst Pressure for Different Tube Diameter (10 ft. Driver Section - Air)

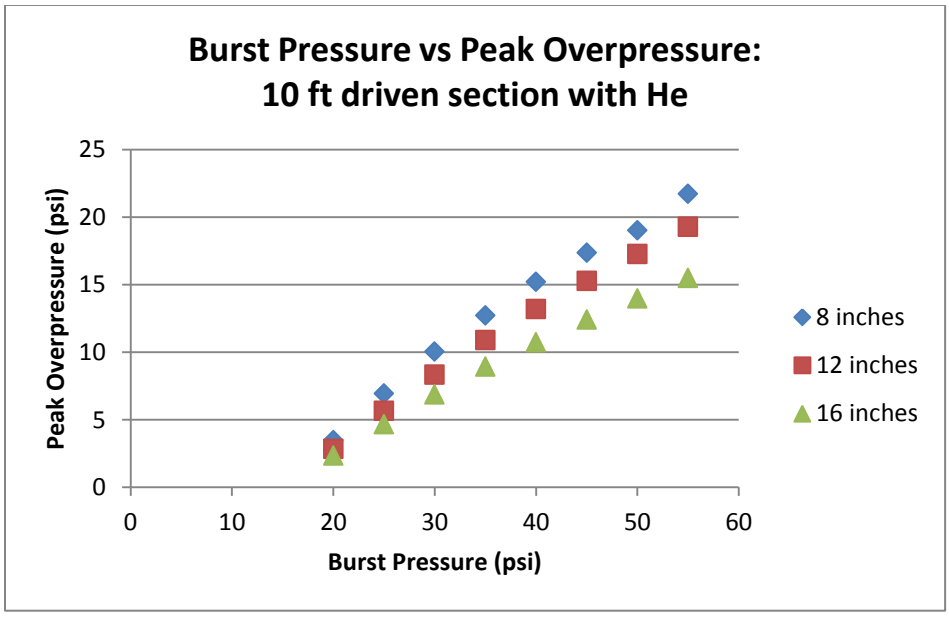

Figure C:4 Comparison of Computational Peak Overpressure Versus Burst Pressure for Different Tube Diameter (10 ft. Driver Section - Helium)

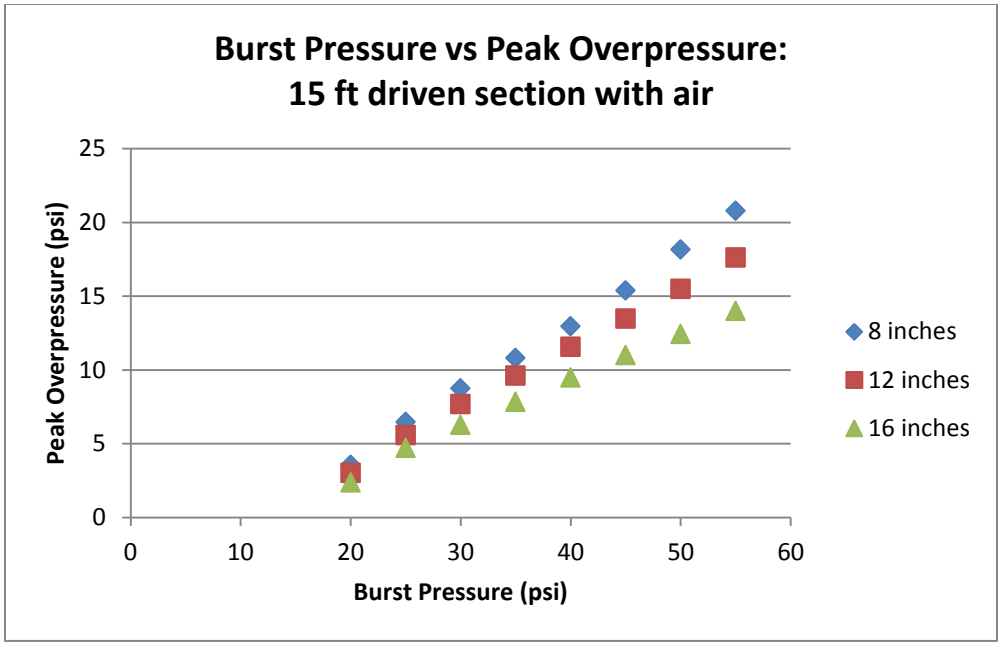

Figure C:5 Comparison of Computational Peak Overpressure Versus Burst Pressure for Different Tube Diameter (15 ft. Driver Section - Air)

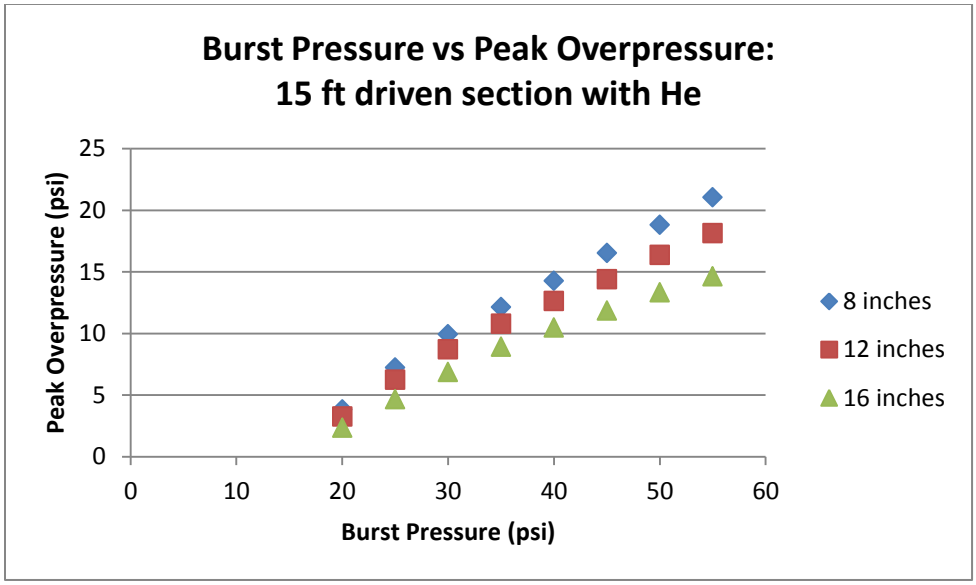

Figure C:6 Comparison of Computational Peak Overpressure Versus Burst Pressure for Different Tube Diameter (15 ft. Driver Section - Helium)

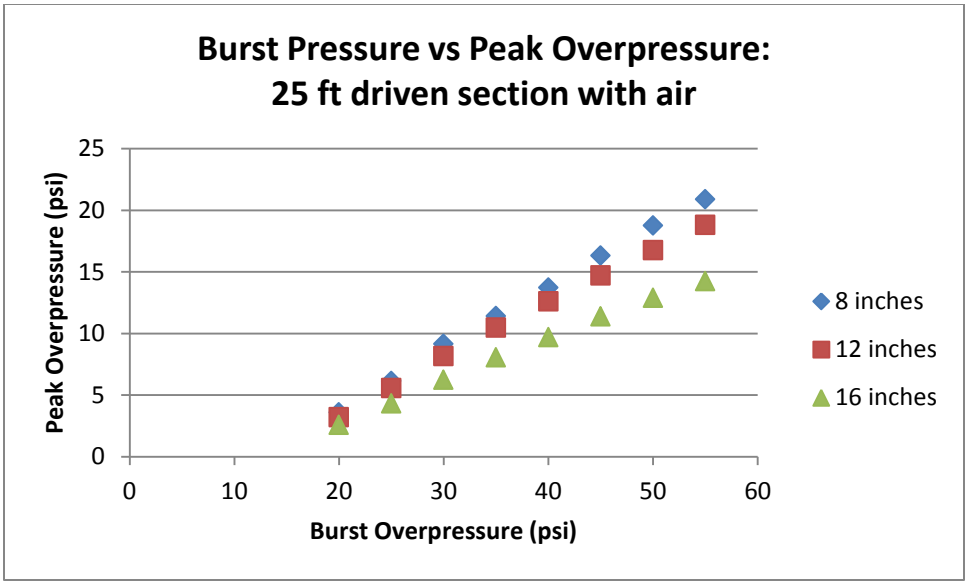

Figure C:7 Comparison of Computational Peak Overpressure Versus Burst Pressure for Different Tube Diameter (25 ft. Driver Section - Air)

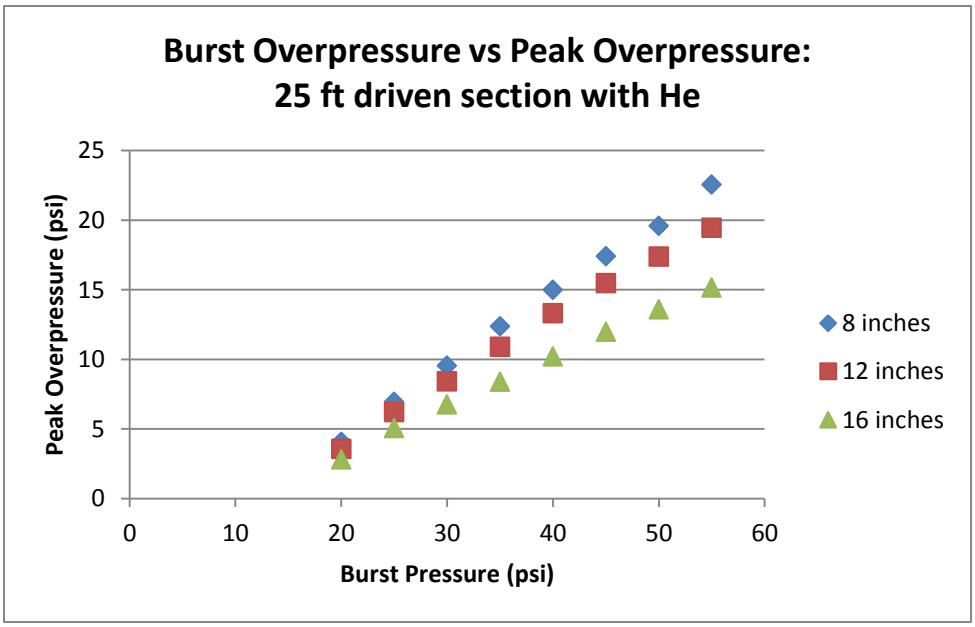

Figure C:8 Comparison of Computational Peak Overpressure Versus Burst Pressure for Different Tube Diameter (25 ft. Driver Section - Helium)

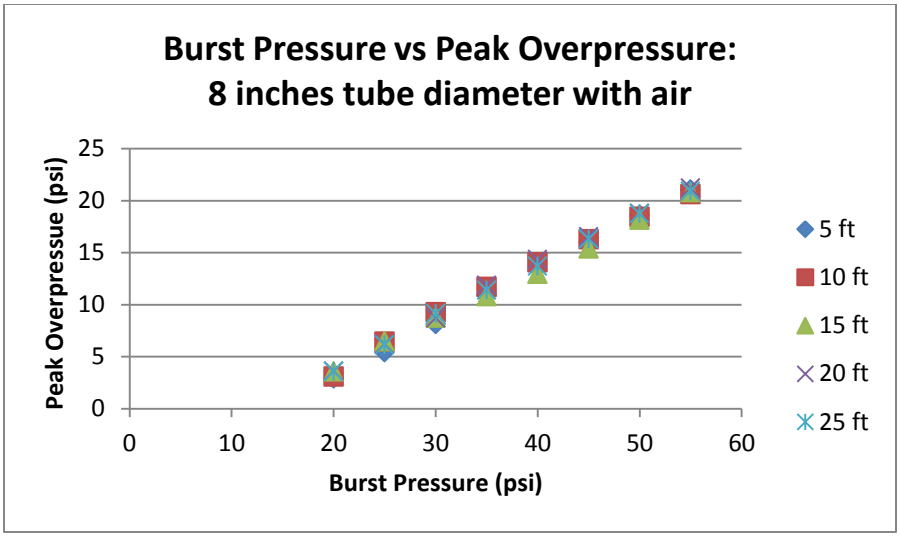

Figure C:9 Comparison of Computational Peak Overpressure Versus Burst Pressure for Different Tube Length (8" Driver Section - Air)

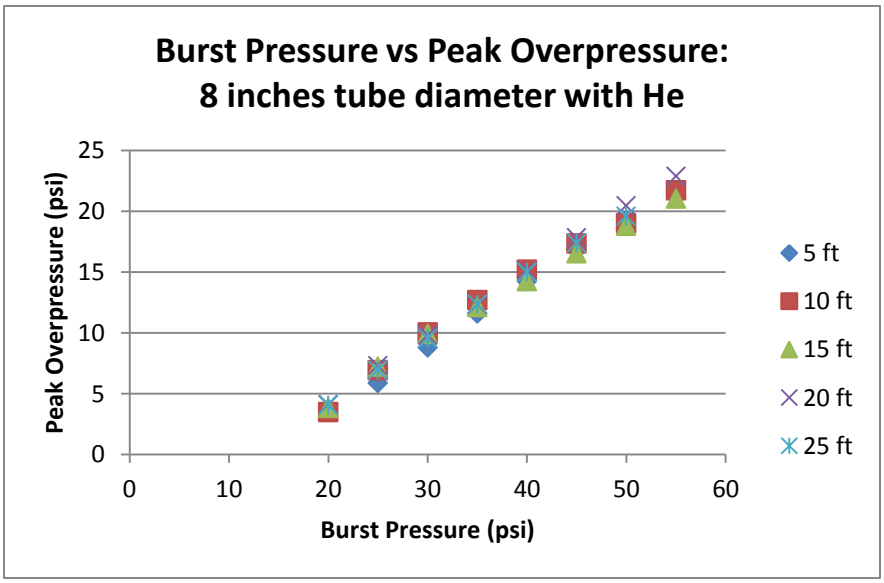

Figure C:10 Comparison of Computational Peak Overpressure Versus Burst Pressure for Different Tube Length (8" Driver Section - Helium)

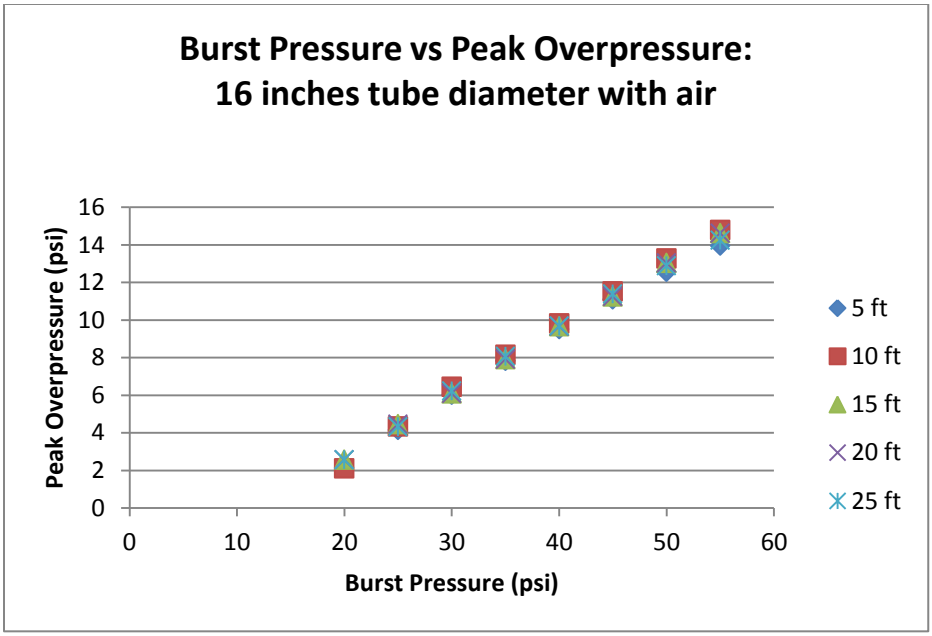

Figure C:11 Comparison of Computational Peak Overpressure Versus Burst Pressure for Different Tube Length (16" Driver Section - Air)

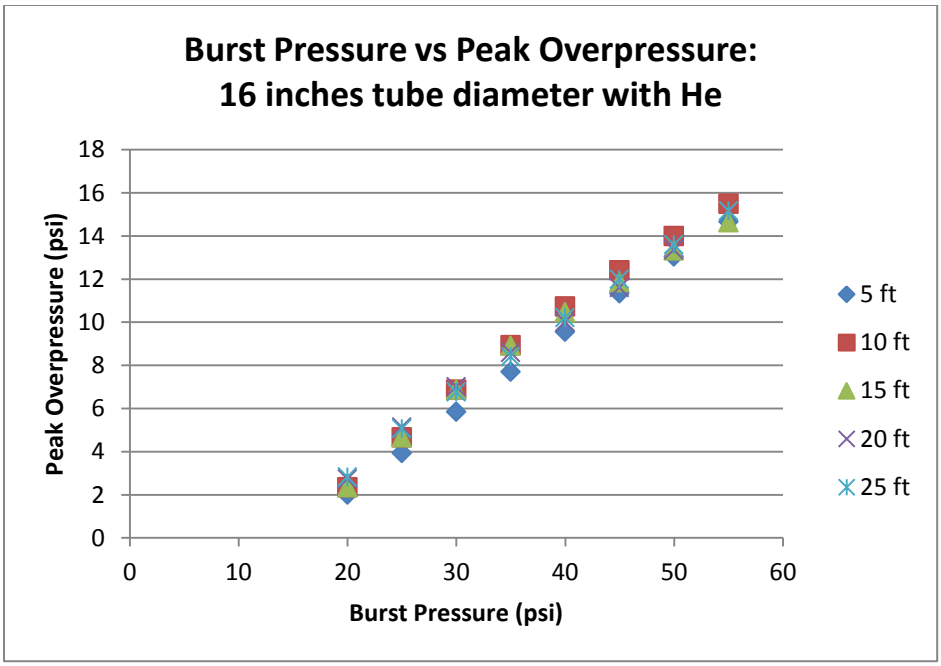

Figure C:12 Comparison of Computational Peak Overpressure Versus Burst Pressure for Different Tube Length (16" Driver Section - Helium)

Table C:7 presents summary of ANOVA analysis for 240 data .

Table C:7 The following table details results of ANOVA for output parameter, peak overpressure, N = 240

Source	DF	Adj SS	Adj MS	F-value	P-Value
Model	13	8463.85	651.07	5042.9	0
Linear	4	8224.18	2056.05	15925.33	0
length	1	11.12	11.12	86.12	0
diameter	1	785.3	785.3	608.6	0.04
gamma	1	32.45	32.45	251.32	0
burst	1	7333.81	7333.81	56804.84	0
Square	3	16.69	5.56	43.1	0
length*length	1	0.84	0.84	6.49	0.011
diameter*diameter	1	2.85	2.85	22.07	0
burst*burst	1	13.33	13.33	103.22	0
2-Way Interaction	6	168.94	28.16	218.09	0
length*diameter	1	0.44	0.44	3.39	0.037

DF - Degrees of freedom from each input

SS - Sum of squares between each input and the sum of squares within each input (error). Adj SS is adjusted to take into consideration all the inputs at different levels

MS – Mean squares are found by dividing the sum of squares by degree of freedom. Adj MS is adjusted to take into consideration all the inputs at different levels

F-value - Calculated by dividing the factor MS by the error MSP - use to determine whether a factor is significant

P-value – Used to determine whether a factor is significant